

## Toward a PV-Based Algorithm for the Dynamical Core of Hydrostatic Global Models

ALI R. MOHEBALHOJEH

*Institute of Geophysics, University of Tehran, Tehran, Iran*

MOHAMMAD JOGHATAEI

*Institute of Geophysics, University of Tehran, Tehran, and Department of Physics,  
Yazd University, Yazd, Iran*

DAVID G. DRITSCHER

*School of Mathematics and Statistics, University of St. Andrews, St. Andrews, United Kingdom*

(Manuscript received 25 October 2015, in final form 16 February 2016)

### ABSTRACT

The diabatic contour-advective semi-Lagrangian (DCASL) algorithms previously constructed for the shallow-water and multilayer Boussinesq primitive equations are extended to multilayer non-Boussinesq equations on the sphere using a hybrid terrain-following–isentropic ( $\sigma$ – $\theta$ ) vertical coordinate. It is shown that the DCASL algorithms face challenges beyond more conventional algorithms in that various types of damping, filtering, and regularization are required for computational stability, and the nonlinearity of the hydrostatic equation in the  $\sigma$ – $\theta$  coordinate causes convergence problems with setting up a semi-implicit time-stepping scheme to reduce computational cost. The prognostic variables are an approximation to the Rossby–Ertel potential vorticity  $Q$ , a scaled pressure thickness, the horizontal divergence, and the surface potential temperature. Results from the DCASL algorithm in two formulations of the  $\sigma$ – $\theta$  coordinate, differing only in the rate at which the vertical coordinate tends to  $\theta$  with increasing height, are assessed using the baroclinic instability test case introduced by Jablonowski and Williamson in 2006. The assessment is based on comparisons with available reference solutions as well as results from two other algorithms derived from the DCASL algorithm: one with a semi-Lagrangian solution for  $Q$  and another with an Eulerian grid-based solution procedure with relative vorticity replacing  $Q$  as the prognostic variable. It is shown that at intermediate resolutions, results comparable to the reference solutions can be obtained.

### 1. Introduction

Construction of potential vorticity (PV)-based models has been the subject of various individual studies (Charney 1962; Bates et al. 1995; Li et al. 2000; Mohebalhojeh and Dritschel 2004). The main objective of such models is to improve the representation of PV and thus simulate vortical flows with higher accuracy than conventional

models. This is important, as vortical flows comprise a significant part of the dynamical phenomena from large scales to mesoscales, including cyclones and fronts (Hoskins et al. 1985; Hsu and Arakawa 1990; Arakawa et al. 1992).

With regard to the material conservation of PV in the absence of diabatic and dissipative processes, it has been noted previously that one may gain higher numerical accuracy and/or computational efficiency by incorporating Lagrangian information within the procedure for time integrating PV. Among these, the contour-advective semi-Lagrangian (CASL) algorithm and its extension to include sources and sinks of PV, that is, the diabatic contour-advective semi-Lagrangian (DCASL) algorithm, have repeatedly shown their potential to increase the accuracy of representing the vortical flow as well as the

---

 Denotes Open Access content.

---

*Corresponding author address:* Ali R. Mohebalhojeh, Institute of Geophysics, University of Tehran, P.O. Box 14155–6466, Tehran 1435944411, Iran.  
E-mail: amohab@ut.ac.ir

DOI: 10.1175/MWR-D-15-0379.1

representation of imbalance (Mohebalhojeh and Dritschel 2007, 2009). Within such numerical algorithms, PV as a defining variable for the vortical flow is given the highest priority in terms of accuracy. The sharp PV gradients generated horizontally by nonlinear advection are captured by CASL/DCASL well beyond the capabilities of conventional grid-based algorithms. This brings with it the necessity of handling small horizontal scales associated with sharp PV gradients. To address this issue, for the  $f$ -plane shallow-water (SW) equations Mohebalhojeh and Dritschel (2000) introduced the idea of implicitly using balance relations (Hoskins et al. 1985; McIntyre and Norton 2000; Mohebalhojeh and Dritschel 2001) through new sets of prognostic variables to represent unbalanced flow, alongside PV as the variable for vortical flow. Since then, the idea has been successfully applied to the SW equations on the sphere (Mohebalhojeh and Dritschel 2007, 2009; MirRokni et al. 2011) and the equatorial  $\beta$  plane (Mohebalhojeh and Theiss 2011), the many-layer isopycnal  $f$ -plane model (Mohebalhojeh and Dritschel 2004), and the two-layer isentropic Boussinesq model on the sphere (Mirzaei et al. 2012). It was also argued in Mohebalhojeh and Dritschel (2004) that in problems involving a large number of layers, the issue with sharp PV gradients is compounded since large shearing motion in the vertical direction tends to generate substantial small-vertical-scale activity in both balanced and unbalanced flows. Associated with this, fictitious generation of imbalance in small vertical scales is inevitable. As a device to gain control on the small vertical scales of imbalance, Mohebalhojeh and Dritschel (2004) introduced and applied the idea of vertical-mode-dependent divergence damping.

Considering both accuracy and computational efficiency, the latter studies have pointed to the pair of horizontal velocity divergence  $\delta$  and horizontal acceleration divergence  $\gamma$  variables, referred to as  $(\delta, \gamma)$ , as a viable candidate for extensions to more complicated sets of equations in our systematic exploration of models. While the non-Boussinesq extension of the two-layer isentropic model of Mirzaei et al. (2012) poses no great difficulty, the use of  $(\delta, \gamma)$  variables has turned out to be hugely more difficult when a generalized vertical coordinate  $\xi$  is used, as discussed below. The problem becomes acute as the number of layers increases to that commonly used in the dynamical core of hydrostatic global models, which is the main objective of our current work. To raise the issues involved, and for continuity with our previous work, aspects of the DCASL algorithm based on the  $(\delta, \gamma)$  variables are presented. However, the focus is on the DCASL algorithm that replaces horizontal acceleration divergence  $\gamma$  with pressure thickness  $\partial p/\partial \xi$ .

The potential temperature  $\theta$  is the other materially conserved quantity in the absence of diabatic and dissipative processes, and it has attracted considerable attention in numerical modeling (Bleck et al. 2010). The layer-wise two-dimensional structure of atmospheric–oceanic flows can be naturally modeled using  $\theta$  as the vertical coordinate. Even though the resulting isentropic models have the potential to give a better representation of baroclinic waves, cyclones, and fronts, the issue of the intersection of isentropic surfaces within the “Underworld,” in the terminology of Hoskins (1991), with bottom topography has proved particularly difficult to resolve. The massless layer approach devised originally by Bleck (1984) gives poor results near the surface (Konor and Arakawa 1997), making it unsuitable for practical purposes when an accurate representation of surface features is needed. Another approach to the problem is to combine one of the terrain-following  $\sigma$  coordinates with the isentropic coordinate in such a way that the resulting hybrid  $\sigma$ – $\theta$  coordinate shares the benefits of  $\sigma$  at lower levels near the ground and  $\theta$  higher up.

Using a hybrid  $\sigma$ – $\theta$  coordinate, Konor and Arakawa (1997) apply both mass continuity and thermodynamic energy equations at half-integer levels and find interpolation relations for the pressure  $p$  and  $\theta$  fields at full (integer) levels from the neighboring half-integer levels, in such a way as to satisfy energy conservation. The vertical mass flux is then obtained by the requirement that the time-discrete solutions for  $p$  and  $\theta$  remain on their defined coordinate surfaces. With the explicit relation defined for the hybrid coordinate, mathematically only the solution to one of the two fields of  $p$  and  $\theta$  is required. The other field can be diagnosed from the definition of the coordinate surface. Here the pressure thickness of the layers is taken as the prognostic variable, and the  $\theta$  field is diagnosed. The vertical differencing remains the same as in Konor and Arakawa (1997), and the vertical mass flux is determined through a diagnostic relation obtained by setting the time derivative of the hybrid vertical coordinate to zero.

The paper is organized as follows. In section 2, the governing equations as well as the formulation of the vertical modes in the generalized vertical coordinate  $\xi$  are presented. Without loss of generality, the analysis is carried out in such a way as to ensure orthogonality of the vertical modes. To this end, a procedure different from the actual vertical differencing employed in the model is followed. Section 3 is devoted to the construction of numerical algorithms and the issues concerning computational damping, vertical differencing, and the setup of the experiments. Section 4 presents results from the DCASL algorithms for the test case of baroclinic instability developed by Jablonowski and

Williamson (2006a). This is a stringent test case for PV-based algorithms, as the instability is concentrated at low levels where the vertical coordinate substantially deviates from  $\theta$  and thus there is a large source coming from vertical advection. Nevertheless, it is shown that the DCASL algorithms at intermediate resolutions can give solutions comparable to the reference solutions in Jablonowski and Williamson (2006a,b) as well as those for a host of other dynamical cores in Lauritzen et al. (2010). Section 5 gives our concluding remarks.

## 2. Formulation

We consider the spherical hydrostatic primitive equations under the shallow-atmosphere approximation (Kasahara 1974; Thuburn 2011) and with continuous stratification represented by a generalized vertical coordinate. In their adiabatic, frictionless form, the governing equations read

$$\frac{D\mathbf{V}}{Dt} + f \hat{\mathbf{k}} \times \mathbf{V} = -\nabla M + \Pi \nabla \theta, \quad (2.1a)$$

$$\frac{\partial M}{\partial \xi} = \Pi \frac{\partial \theta}{\partial \xi}, \quad (2.1b)$$

$$\frac{\partial}{\partial t} \left( \frac{\partial p}{\partial \xi} \right) + \nabla \cdot \left( \mathbf{V} \frac{\partial p}{\partial \xi} \right) + \frac{\partial}{\partial \xi} \left( \dot{\xi} \frac{\partial p}{\partial \xi} \right) = 0, \quad \text{and} \quad (2.1c)$$

$$\frac{D\theta}{Dt} = 0, \quad (2.1d)$$

where  $D/Dt \equiv \partial/\partial t + \mathbf{V} \cdot \nabla + \dot{\xi} \partial/\partial \xi$  is the material derivative,  $\mathbf{V}$  is the horizontal velocity vector,  $f = 2\Omega_E \sin\phi$  is the Coriolis parameter with  $\Omega_E$  being the rotation rate of the sphere and  $\phi$  being the latitude,  $\hat{\mathbf{k}}$  is the unit vector in the local vertical direction,  $M$  is the Montgomery potential,  $\theta$  is potential temperature,  $\xi$  is the generalized vertical coordinate with  $\dot{\xi}$  its associated vertical velocity, and  $\Pi \equiv c_p(p/p_0)^\kappa$  is the Exner function with  $\kappa = R/c_p$ . Here,  $R$  and  $c_p$  are the gas constant and specific heat capacity at constant pressure for dry air. In (2.1) and hereafter, the  $\nabla$  and  $\nabla \cdot$  are, respectively, the horizontal gradient and divergence operators.

To define vertical modes and construct a semi-implicit time integration scheme, a resting basic state in hydrostatic balance is defined whose variables are denoted by an overbar. The basic state is considered a function of the vertical coordinate only. Any variable can be decomposed into a contribution from the basic state and a perturbation; thus, for example,  $\Pi = \bar{\Pi} + \Pi'$ . In this way, the right-hand side of (2.1a) can be written as  $-\nabla P' + \Pi' \nabla \theta'$ , where  $P = M - \bar{\Pi} \theta$ ,  $P' = M' - \bar{\Pi} \theta' = \Phi' + \Pi' \theta$ , with  $\Phi$  being the geopotential. For reference, hereafter  $P'$  is called ‘‘modified pressure.’’ By defining a nondimensional perturbation depth or pressure thickness

variable  $\tilde{h}$  through  $\partial p/\partial \xi = \partial \bar{p}/\partial \xi (1 + \tilde{h})$ , it is convenient to rewrite the mass continuity equation [(2.1c)] as

$$\frac{\partial \tilde{h}}{\partial t} + \nabla \cdot [\mathbf{V}(1 + \tilde{h})] + \frac{1}{\partial \bar{p}} \frac{\partial}{\partial \xi} \left( \dot{\xi} \frac{\partial p}{\partial \xi} \right) = 0, \quad (2.2)$$

to bring it into the same form used in the SW equations with an apparent source due to vertical mass flux divergence.

### a. Vertical modes

Following Temperton (1984), the primitive equations linearized around a basic state at rest are recast in the form of the SW equations by finding a matrix  $\mathbf{C}$  such that

$$\frac{\partial \mathbf{P}'}{\partial t} = -\mathbf{C} \boldsymbol{\delta}, \quad (2.3)$$

where  $\mathbf{P}'$  is the column vector  $(P'_1, P'_2, \dots, P'_L)^T$  with  $L$  being the number of layers and the T denoting transpose. The column vector  $\boldsymbol{\delta}$  of the horizontal divergence is defined similarly. While it is possible to obtain the discrete analog of (2.3) for the vertical differencing of Konor and Arakawa (1997) given later in section 3c, we will follow a different route. The reason is that, by following Konor and Arakawa (1997), the resulting matrix  $\mathbf{C}$  is nonsymmetric, and the vertical modes are non-orthogonal for arbitrary stratification of the basic state. Here, instead, we first find the continuous equation for the time tendency of  $P'$  and then vertically discretize it in such a way as to ensure  $\mathbf{C}$  is symmetric. For our purpose the vertical modes serve as a set of basis functions with desirable properties that help control small-scale vertical structures, help solve the elliptic equation arising when the  $(Q, \delta, \gamma)$  representation is used, and facilitate a semi-implicit solution procedure.

To obtain the matrix formulation, we write the vertical derivative of the tendency of  $P'$  as

$$\frac{\partial}{\partial \xi} \frac{\partial P'}{\partial t} = H. \quad (2.4)$$

To find the right-hand side function  $H$ , the hydrostatic equation [(2.1b)] is first written as

$$\frac{\partial P'}{\partial \xi} = \Pi' \frac{\partial \theta}{\partial \xi} - \theta' \frac{\partial \bar{\Pi}}{\partial \xi}, \quad (2.5)$$

and then time differentiated, which after some manipulation leads to

$$H = \left( \kappa \frac{\Pi}{p} \frac{\partial \theta}{\partial \xi} \right) \frac{\partial p'}{\partial t} - \frac{\partial \bar{\Pi}}{\partial \xi} \frac{\partial \theta'}{\partial t} + \Pi' \frac{\partial}{\partial \xi} \frac{\partial \theta'}{\partial t}. \quad (2.6)$$

The following well-known forms of the pressure vertical velocity  $\omega$ ,

$$\omega = \frac{\partial p'}{\partial t} + \mathbf{V} \cdot \nabla p + \xi \frac{\partial p}{\partial \xi}, \tag{2.7}$$

$$\omega = \mathbf{V} \cdot \nabla p + \hat{\omega}, \quad \text{and} \tag{2.8}$$

$$\hat{\omega} = - \int_{\xi_{\text{top}}}^{\xi} \nabla \cdot \left( \mathbf{V} \frac{\partial p}{\partial \xi} \right) d\xi, \tag{2.9}$$

with  $\xi_{\text{top}}$  the value of  $\xi$  at the top of the model and  $\hat{\omega}$  as an auxiliary variable, are used to rewrite the thermodynamic energy equation [(2.1d)] as

$$\frac{\partial \theta'}{\partial t} = -\mathbf{V} \cdot \nabla \theta' - \frac{\partial \theta}{\partial \xi} \frac{\partial \theta'}{\partial p} \left( \hat{\omega} - \frac{\partial p'}{\partial t} \right). \tag{2.10}$$

Noting that  $\kappa \Pi / p = \partial \Pi / \partial p$ , we can then write  $H$  as

$$H = \frac{\partial \Pi'}{\partial p} \frac{\partial \theta}{\partial \xi} \frac{\partial p'}{\partial t} + \frac{\partial \bar{\Pi}}{\partial p} \frac{\partial \theta}{\partial \xi} \hat{\omega} + \frac{\partial \bar{\Pi}}{\partial \xi} \mathbf{V} \cdot \nabla \theta' + \Pi' \frac{\partial}{\partial \xi} \frac{\partial \theta'}{\partial \xi}. \tag{2.11}$$

Then, we multiply (2.4) by  $\partial \xi / \partial p$  and vertically integrate the result from the middle of the layer with pressure  $p$  to the surface with pressure  $p_s$

$$\frac{\partial P'}{\partial t} = \frac{\partial P'_s}{\partial t} - \int_p^{p_s} H \frac{\partial \xi}{\partial p} dp. \tag{2.12}$$

In  $P'_s$  and similar terms, the subscript  $s$  refers to the surface value of the quantity. The surface term on the right-hand side of (2.12) can be written as

$$\begin{aligned} \frac{\partial P'_s}{\partial t} &= -\Pi' \mathbf{V}_s \cdot \nabla \theta' + \frac{RT_s}{p_s} \frac{\partial p_s}{\partial t} \\ &= -\Pi' \mathbf{V}_s \cdot \nabla \theta' - \frac{RT_s}{p_s} \int_{\xi_{\text{top}}}^{\xi_s} \nabla \cdot \left( \mathbf{V} \frac{\partial p}{\partial \xi} \right) d\xi. \end{aligned} \tag{2.13}$$

Defining  $\mathbf{G}$  and  $\mathbf{H}$  as the column vectors of, respectively,  $\partial P' / \partial t$  and  $H \partial \xi / \partial p$ , (2.12) can be written in matrix form as

$$\mathbf{G} = \mathbf{G}_s - \mathbf{A}\mathbf{H}, \tag{2.14}$$

where

$$\mathbf{A} = \begin{bmatrix} \frac{(\Delta \bar{p})_1}{2} & (\Delta \bar{p})_2 & \dots & (\Delta \bar{p})_L \\ 0 & \frac{(\Delta \bar{p})_2}{2} & \dots & (\Delta \bar{p})_L \\ 0 & 0 & \ddots & \vdots \\ 0 & 0 & \dots & \frac{(\Delta \bar{p})_L}{2} \end{bmatrix} = \mathbf{U} \text{diag}[(\Delta \bar{p})] \quad \text{and} \tag{2.15}$$

$$\mathbf{G}_s = G_s(1, 1, \dots, 1)^T, \tag{2.16}$$

in which  $\text{diag}[(\Delta \bar{p})]$  is the diagonal matrix whose elements are  $(\Delta \bar{p})_1, (\Delta \bar{p})_2, \dots, (\Delta \bar{p})_L$  with  $(\Delta \bar{p})_l = \bar{p}_{l+1/2} - \bar{p}_{l-1/2}$ . The vectors  $\mathbf{G}_s$  and  $\mathbf{H}$  can be decomposed into linear and nonlinear parts, that is  $\mathbf{G}_s = \mathbf{G}_{s,l} + \mathbf{G}_{s,nl}$  and  $\mathbf{H} = \mathbf{H}_l + \mathbf{H}_{nl}$ , where

$$\mathbf{G}_{s,l} = -\frac{R\bar{T}_s}{\bar{p}_s} \mathbf{E} \text{diag}[(\Delta \bar{p})] \boldsymbol{\delta} \quad \text{and} \tag{2.17}$$

$$\mathbf{H}_l = -\text{diag} \left( \frac{\Delta \bar{\Pi}}{\Delta \bar{p}} \right) \frac{\partial \bar{\theta}}{\partial p} \mathbf{L} \text{diag}[(\Delta \bar{p})] \boldsymbol{\delta}, \tag{2.18}$$

with  $(\Delta \bar{\Pi})_l = \bar{\Pi}_{l+1/2} - \bar{\Pi}_{l-1/2}$ . Here,  $\mathbf{G}_{s,l}$  and  $\mathbf{H}_l$  result from manipulating the second terms on the right-hand sides of, respectively, (2.13) and (2.11). The upper and lower triangular matrices  $\mathbf{U}$  and  $\mathbf{L}$  are defined by

$$\mathbf{U} = \begin{pmatrix} \frac{1}{2} & 1 & \dots & 1 \\ 0 & \frac{1}{2} & \dots & 1 \\ 0 & 0 & \ddots & \vdots \\ 0 & 0 & \dots & \frac{1}{2} \end{pmatrix} \quad \text{and} \tag{2.19}$$

$$\mathbf{L} = \begin{pmatrix} \frac{1}{2} & 0 & \dots & 0 \\ 1 & \frac{1}{2} & \dots & 0 \\ \vdots & 1 & \ddots & 0 \\ 1 & 1 & \dots & \frac{1}{2} \end{pmatrix}, \tag{2.20}$$

and the matrix  $\mathbf{E}$  has 1 for every element. Using (2.14), one can obtain the matrix  $\mathbf{C}$  as

$$\mathbf{C} = \left\{ \frac{R\bar{T}_s}{\bar{p}_s} \mathbf{E} - \mathbf{U} \text{diag} \left[ \frac{\partial \bar{\Pi}}{\partial p} (\Delta \bar{p}) \frac{\partial \bar{\theta}}{\partial p} \right] \mathbf{L} \right\} \text{diag}[(\Delta \bar{p})], \tag{2.21}$$

which is the generalization of the matrix (2.34) of Temperton (1984) for  $\sigma$ -coordinate models. In this way the matrix  $\mathbf{C}$  can be determined by the basic-state pressure and potential temperature distributions at half-integer levels. For the particular case of  $\xi = \theta$ , for which the question of vertical differencing becomes trivial, (2.21) can be regarded as a generalization of the matrix obtained in Mirzaei et al. (2012) for the Boussinesq equations. It is worth noting that in obtaining the

matrix formulation, the vertical discretization only comes into play in approximating the integrals involved in (2.12) and in the linearized form of (2.9), for which the midpoint rule is used together with the approximation  $\bar{p}_l = (\bar{p}_{l+1/2} + \bar{p}_{l-1/2})/2$  to reach a symmetric matrix. It should be stressed that there is no conflict in making the above choice for the full-level basic-state pressure  $\bar{p}$  and using the pressure  $p$  coming from the relation (3.16b) introduced later for the actual vertical differencing of the model.

Any matrix of the form  $\mathbf{UDL}$  with  $\mathbf{D}$  as a diagonal matrix is symmetric. This property and symmetry of  $\mathbf{E}$  make  $\mathbf{C}$  symmetric. The eigenvectors and eigenvalues of the matrix  $\mathbf{C}$  are used to define the vertical modes and vertical-mode decomposition. To this end, the decomposition  $\mathbf{C} = \mathbf{W}\mathbf{\Lambda}\mathbf{W}^{-1}$  is employed, where  $\mathbf{W}$  and  $\mathbf{\Lambda}$  are, respectively, the matrix of eigenvectors and the diagonal matrix of eigenvalues of  $\mathbf{C}$ . For a general column vector  $\mathbf{X}$  in physical space, its projection onto the vertical mode space is defined by  $\tilde{\mathbf{X}} = \mathbf{W}^{-1}\mathbf{X}$ .

Let us define a column vector  $\mathbf{h}$ , not to be confused with the perturbation depth variable  $\tilde{h}$ , by  $\mathbf{h} = \mathbf{C}^{-1}\mathbf{P}'$ . Now note that  $\tilde{\mathbf{h}} = \mathbf{W}^{-1}(\mathbf{W}\mathbf{\Lambda}^{-1}\mathbf{W}^{-1})\mathbf{P}'$  and thus  $\tilde{h}_m = \lambda_m^{-1}\tilde{P}'_m$  for the vertical mode  $m$  with the eigenvalue  $\lambda_m$ . The momentum equation [(2.1a)] linearized around the resting basic state together with (2.3) then become equivalent to the linearized SW equations upon projection to vertical modes:

$$\frac{\partial \tilde{\mathbf{V}}'}{\partial t} + f\hat{\mathbf{k}} \times \tilde{\mathbf{V}}' = -\Lambda\nabla\tilde{\mathbf{h}} \quad \text{and} \quad (2.22a)$$

$$\frac{\partial \tilde{\mathbf{h}}}{\partial t} = -\tilde{\delta}. \quad (2.22b)$$

It is now evident from (2.22) that we can identify the eigenvalues with the squared gravity wave speeds in the shortwave limit, namely,  $\lambda_m = c_m^2$ .

*b. Vertical velocity*

To evaluate the time tendency of modified pressure from (2.4) and (2.6), the generalized vertical velocity  $\dot{\xi}$  is required. Taking the local time derivative of  $\xi = F(\sigma, \theta)$ , with  $\sigma$  defined according to

$$\sigma = \frac{p_s - p}{p_s - p_{\text{top}}}, \quad (2.23)$$

the following diagnostic equation can be obtained

$$\dot{\xi} = -\frac{1}{p_s - p_{\text{top}}} \left\{ \left[ \hat{\omega} - (1 - \sigma) \frac{\partial p_s}{\partial t} \right] \frac{\partial F}{\partial \sigma} \right\} - \frac{\partial F}{\partial \theta} \mathbf{V} \cdot \nabla \theta. \quad (2.24)$$

In (2.23),  $p_s$  is the surface pressure,  $p_{\text{top}}$  is the pressure at the top of the model, and  $\partial p_s / \partial t = \hat{\omega}(\xi_s)$  is computed diagnostically from (2.9). For conservation of total energy, in deriving (2.24)  $p_{\text{top}}$  has taken to be constant (see Konor and Arakawa 1997). One may also take the total derivative of  $\xi = F(\sigma, \theta)$  and come up with the alternative form  $\dot{\xi} = (\partial F / \partial \sigma) \dot{\sigma}$  for vertical velocity. Using the identity  $\nabla \xi = 0$ , which holds on  $\xi$  surfaces, it is not difficult to show that the latter form and (2.24) are equivalent in the continuous limit. The time tendency of modified pressure also requires the time tendency of pressure, which is evaluated using

$$\frac{\partial p'}{\partial t} = \hat{\omega} - \dot{\xi} \frac{\partial p}{\partial \xi}. \quad (2.25)$$

One potential problem with the use of the diagnostic estimate for  $\dot{\xi}$  is that an independent estimate for  $\partial p / \partial \xi$  is then required at half-integer levels where  $\dot{\xi}$  resides. Alternatively, the same procedure leading to (2.24) can be modified to give us directly a diagnostic estimate for the vertical mass flux  $\dot{\xi} \partial p / \partial \xi$ . The resulting diagnostic estimate for the vertical mass flux, which will be presented as part of the vertical differencing, constitutes an essential part of the algorithms described next.

**3. Numerical algorithms**

For the primitive equations using the hybrid  $\sigma$ - $\theta$  vertical coordinate  $\xi$ , the multilayer counterpart of the type-I DCASL algorithms described in Mohebalhojeh and Dritschel (2009) have been developed. The algorithms use the prognostic variable  $Q \equiv (f + \zeta)/(1 + \tilde{h})$  alongside either the variables  $\tilde{h}$  and horizontal divergence  $\delta$ , leading to what is called here  $CA_{\tilde{h},\delta}$ , or the variables  $\delta$  and  $\gamma \equiv f\zeta - \nabla^2 P - \beta u$  leading to the algorithm  $CA_{\delta,\gamma}$ . In the definition of  $\gamma$ ,  $\zeta$  is the relative vorticity,  $\beta$  is the northward gradient of  $f$ , and  $u$  is the velocity component in the longitudinal ( $\lambda$ ) direction. Whenever  $\xi$  tends to  $\theta$ , the PV-like variable  $Q$  tends to the Rossby-Ertel PV, and the variable  $\gamma$  tends to horizontal acceleration divergence, exactly as in the SW equations and in the primitive equations with  $\theta$  as the vertical coordinate. For  $CA_{\delta,\gamma}$ , the prognostic equations read

$$\frac{D_h Q}{Dt} = Q \left\{ \frac{1}{\frac{\partial \bar{p}}{\partial \xi}} \frac{\partial}{\partial \xi} \left( \dot{\xi} \frac{\partial p}{\partial \xi} \right) - \frac{1}{f + \zeta} \left[ \hat{\mathbf{k}} \cdot \nabla \times \left( \dot{\xi} \frac{\partial u}{\partial \xi} - \frac{\pi'}{\cos \phi} \frac{\partial \theta'}{\partial \lambda}, \dot{\xi} \frac{\partial v}{\partial \xi} - \pi' \frac{\partial \theta'}{\partial \phi} \right) \right] \right\}, \quad (3.1)$$

$$\frac{\partial \delta}{\partial t} = \gamma - 2 \left[ \frac{\partial u}{a \partial \phi} \left( \frac{\partial u}{a \partial \phi} + \zeta \right) + \frac{\partial v}{a \partial \phi} \left( \frac{\partial v}{a \partial \phi} - \delta \right) \right] - \nabla \cdot (\delta \mathbf{V}) - \frac{|\mathbf{V}|^2}{a^2} + \left[ \nabla \cdot \left( \pi' \nabla \theta' - \xi \frac{\partial \mathbf{V}}{\partial \xi} \right) \right] + \mathcal{D}(\delta), \quad \text{and} \quad (3.2)$$

$$\frac{\partial \tilde{\gamma}}{\partial t} = \underbrace{c_m^2 \nabla^2 \tilde{\delta} - \nabla^2 N + \frac{2\Omega_E}{a^2} \frac{\partial B}{\partial \lambda} - \nabla \cdot (Z\mathbf{V})}_{\text{left-hand side}} \left\{ -f \left[ \hat{\mathbf{k}} \cdot \nabla \times \left( \xi \frac{\partial u}{\partial \xi} - \frac{\pi'}{\cos \phi} \frac{\partial \theta'}{\partial \lambda}, \xi \frac{\partial v}{\partial \xi} - \pi' \frac{\partial \theta'}{\partial \phi} \right) \right] + \beta \left( \xi \frac{\partial u}{\partial \xi} - \frac{\pi'}{\cos \phi} \frac{\partial \theta'}{\partial \lambda} \right) \right\}, \quad (3.3)$$

where  $D_h/Dt \equiv \partial/\partial t + \mathbf{V} \cdot \nabla$  is the material derivative following two-dimensional motion on  $\xi$  surfaces,  $v$  is the velocity component in the latitudinal ( $\phi$ ) direction,  $Z = f(f + \zeta)$ ,  $B \equiv P' + (1/2)|\mathbf{V}|^2$  is the Bernoulli pressure, and  $a$  is the Earth's radius. To make it as similar as possible to the SW equations, (3.3) has been written in vertical-mode space in which  $m$  is the mode number and  $N$  denotes the sum of nonlinear terms in the time tendency of modified pressure  $P'$ :

$$\frac{\partial \mathbf{P}'}{\partial t} = -\mathbf{C}\delta + \mathbf{N}. \quad (3.4)$$

Note that upon projection to vertical modes,  $\mathbf{C}\delta$  becomes  $\Lambda \tilde{\delta}$  where  $\Lambda = \text{diag}(c_m^2)$ . Further, the terms arising from the deviation of  $\xi$  from  $\theta$  have been grouped together in the curly bracket on the right-hand sides of (3.1)–(3.3). The damping operator  $\mathcal{D}$  included in the last term on the right-hand side of (3.2) will be explained later in this section. Using the earth's radius  $m$  as the horizontal length scale and one day  $T_{\text{day}} = 2\pi/\Omega_E$  with  $s^{-1}$  as the time scale, a proper nondimensionalization of the equations is obtained from which we can set  $a = 1$ ,  $\Omega = 2\pi$ ,  $f = 4\pi \sin \phi$ , and  $\beta = 4\pi \cos \phi$  in (3.2) and (3.3) as well as in the definition of the variables  $(Q, \delta, \gamma)$ .

In the DCASL algorithms, the  $Q$  field is partitioned into an adiabatic part  $Q_a$  and a diabatic part  $Q_d$  by writing  $Q = Q_a + Q_d$  and setting

$$\frac{D_h Q_a}{Dt} = 0 \quad \text{and} \quad \frac{D_h Q_d}{Dt} = S_Q, \quad (3.5)$$

where  $S_Q$  denotes the right-hand side of (3.1). Note that in the adiabatic form of the primitive equations, there is no true diabatic source for  $Q_d$ . However, for consistency with the general use of DCASL, it is preferable to call  $Q_d$  the diabatic part. The  $Q_a$  field is solved using the spherical extension of the CASL algorithm (Dritschel and Ambaum 1997), which simply combines a contour representation with contour advection, facilitated by a novel, fast contour-to-grid conversion. Critical to this conversion is the assumption of a piecewise uniform

distribution for  $Q_a$ , where the contours define the level sets or jumps of  $Q_a$ . In this sense, a contour representation is distinct from using contours to illustrate a field (for a full description, see Dritschel and Ambaum 1997; Mohebalhojeh and Dritschel 2009). The forced advection equation for  $Q_d$  given in (3.5) is solved using a standard semi-Lagrangian method, the most important feature of which is a piecewise bicubic Lagrange interpolation to compute  $Q_d$  and  $S_Q$  at the departure points of the back trajectories involved.

The equations for the variables  $(\delta, \gamma)$  and  $(\tilde{h}, \delta)$  used alongside  $Q$  are solved using spectral transforms in longitude, fourth-order compact differencing in latitude (Mohebalhojeh and Dritschel 2007), and a three-time-level time-stepping scheme. For  $(\delta, \gamma)$ , a semi-implicit scheme is implemented that follows Mohebalhojeh and Dritschel (2004). The  $(\delta, \gamma)$  algorithm involves an inversion procedure to find  $\tilde{h}$  and the thermodynamic variables from  $(Q, \delta, \gamma)$ , details of which are given in appendix A. The inversion procedure has been successfully applied in the two-layer non-Boussinesq counterpart of experiments similar to those carried out in Mirzaei et al. (2012) to examine the degree of imbalance generated during the evolution of vortical flows. It turns out, however, that the solution procedure fails to converge when the number of layers increases. What impedes convergence is the nonlinearity of the hydrostatic equation [(2.1b)] when use is made of the hybrid coordinate  $\xi$ . An algorithm intermediate between  $CA_{\tilde{h}, \delta}$  and  $CA_{\delta, \gamma}$ , using the variables  $(P, \delta)$  has also been constructed for which the same semi-implicit time-stepping scheme of  $CA_{\delta, \gamma}$  is applicable. This algorithm requires a fast inversion of modified pressure at each gridpoint column to recover the thermodynamic variables. The iterative algorithm described in appendix A loses efficiency and convergence for a large number of layers for the same reason alluded to above for the inversion of  $\gamma$ . For the numerical results presented in this paper, we have thus been restricted to the  $(\tilde{h}, \delta)$  variables with an explicit leapfrog time differencing scheme. In the rest of the paper, the latter algorithm is referred to as CA.

To provide a basis for comparison, two other algorithms are derived from the CA algorithm thus described. The first, called SL for reference, differs from the CA only in that it solves (3.1) for  $Q$  using the same semi-Lagrangian method employed in CA for  $Q_a$ . The second, called PS for reference, is a vorticity–divergence-based algorithm. The solution procedure for  $\tilde{h}$  and  $\delta$  is exactly as in the CA and SL algorithms, but instead of  $Q$ , the prognostic equation for  $\zeta$  (not shown for brevity) is solved like that for  $\delta$  in a pseudospectral manner.

*a. Computational damping*

To deal with the grid-scale structures generated as a result of both the inevitable direct cascade to smaller scales and computational errors, one has to equip the algorithms with suitable forms of damping, or more generally, regularization techniques. Here, an account of the damping techniques employed is given.

- 1) The application of the sixth-order filter (C.2.8) of Lele (1992) to  $\delta$  and  $\xi\partial p/\partial\xi$  and the eighth-order filter by Cook and Cabot (2005) to  $\tilde{h}$  in both the zonal and meridional directions. In PS, for long-term numerical stability the sixth-order filter is applied to all of the prognostic variables as well as to the mass flux. Details of the filters will be presented later where it will be shown that they are effective in suppressing the two-grid-interval noise generated by the compact meridional differencing (for which, see the analysis and results in section 3.3.4 of Durran 2010).
- 2) The application of a steep spectral filter due to Broutman (Smith and Dritschel 2006) in the zonal direction to the time tendencies of  $\delta$  and  $\tilde{h}$  as well as to the mass flux  $\xi\partial p/\partial\xi$  as a form of de-aliasing.
- 3) A vertical-mode-dependent divergence damping by application of the diffusion operator to the horizontal divergence. Following Mohebalhojeh and Dritschel (2004), this is carried out to control fictitious generation of imbalance that can lead to numerical instability.
- 4) A Robert–Asselin (RA) filter or its modification called RAW (Williams 2009, 2011) to damp the computational mode of the leapfrog scheme. The filter is applied to  $\delta$  in CA and SL and to  $\zeta$  and  $\delta$  in PS. The results presented in this work are using the RA filter.
- 5) The pole problem is dealt with by application of the ideal second-order Shapiro filter (see Jablonowski and Williamson 2011 for details) to the horizontal divergence and vertical mass flux at the grid circle nearest to each pole.
- 6) Application of convective adjustment to regularize the vertical velocity field and thus coordinate surfaces by removing regions of static instability. There

are two procedures implemented for convective adjustment: (i) a fixed number of iterations of the procedure presented by Konor and Arakawa (1997) and (ii) a convergent algorithm introduced by Akmaev (1991). With an eye on the extension to nonhydrostatic global models, work is also under way to meet the requirement for regularization of the coordinate surfaces by replacing the convective adjustment with the implementation of an adaptive vertical grid following the “arbitrary Lagrangian–Eulerian” method (Toy and Randall 2009; Bleck et al. 2010).

- 7) An adjustment of the vertical mass flux to ensure the layer pressure thickness remains above a predefined level equal to  $0.02\Delta\bar{p}$ . The combined spectral in longitude and compact in latitude algorithm used to solve the mass continuity equation can lead to undershoots and overshoots in the presence of sharp gradients. Numerical experiments show that the fictitious extrema of the depth field thus generated can also lead to localized excessively large values of the source term for  $Q$ , that is,  $S_Q$ , in both CA and SL. Therefore, further control is provided by the application of Rayleigh damping to the depth and  $Q$  fields at those points where  $\tilde{h}$  and/or  $S_Q$  go outside the intervals  $[-0.9, 4]$  and  $[-500, 500]$  in nondimensional units, respectively. It is worth mentioning that the latter choices for the intervals are rather conservative and wider intervals are also possible. In the PS algorithm, in cases where  $\tilde{h}$  goes outside the interval  $[-0.9, 4]$ , the local damping is applied to the depth and vorticity fields. Such measures are analogous to the local vertical momentum diffusion employed by Konor and Arakawa (1997).
- 8) In CA,  $Q$  is regularized by contour surgery (Dritschel 1988, 1989; Dritschel and Ambaum 1997) applied to the contour representation of  $Q_a$ . There is also inherent damping of  $Q_a$  arising from the semi-Lagrangian method employed. The latter is the sole damping of  $Q$  in the SL algorithm.

*b. Filter properties*

When the leapfrog scheme is used for the time discretization of the undamped divergence equation, linear stability can be maintained irrespective of the strength of damping if the damping term on the right-hand side of (3.2) is solved using a backward scheme (Durran 2010),

$$\delta^{n+1} = \delta^{*n+1} + 2\Delta t \mathcal{D}(\delta^{n+1}), \tag{3.6}$$

where  $\delta^{*n+1}$  is the solution at time level  $n + 1$  of the undamped divergence equation [(3.2)]. The solution at time level  $n + 1$  can then be written as

$$\delta^{n+1} = (1 - 2\Delta t \mathcal{D})^{-1} \delta^{*n+1}. \tag{3.7}$$

For the implicit operator  $(1 - 2\Delta t \mathcal{D})^{-1}$ , what we have at our disposal is nothing but a filtering operation. More generally, we can write

$$\delta^{n+1} = \mathcal{F} \delta^{*n+1}, \tag{3.8}$$

where  $\mathcal{F}$  represents a spatial filter with desirable properties.

In this work, we have examined two kinds of spatial filter. The first kind corresponds to the class of continuous filters coming from differential operators  $\mathcal{D}$  of diffusion type. A well-known example is  $\mathcal{D}_m = \nu_m \nabla^2$ , where  $\nu_m$  is the diffusion coefficient for the  $m$ th vertical mode. By inclusion of the index  $m$  in  $\nu$ , allowance has been made for a vertical-mode-dependent damping. The diffusion coefficient is set to

$$\nu_m = \frac{1}{\tau} \left( \frac{1}{l_{\max}} \frac{\Delta \phi}{L_{R,m}} \right)^2, \tag{3.9}$$

where  $L_{R,m} = c_m / (2\Omega)$  is the Rossby radius of vertical mode  $m$  based on the polar value of the Coriolis parameter,  $l_{\max}$  is the maximum wavenumber in the meridional direction, and  $\tau$  is the damping time of the shortest resolvable wave of the vertical mode with  $L_{R,m} = \Delta \phi$  in nondimensional units. The underlying reason for the use of harmonic diffusion on  $\delta$  is that the fictitious generation of imbalance due to large vertical shear induced by horizontal advection of  $Q$  is spread across scales (Mohebalhojeh and Dritschel 2004). In the PS algorithm, independent of vertical mode, the diffusion coefficient is set to  $\nu = 1/(\tau l_{\max}^2)$ .

The second kind of spatial filter consists of the class of discrete filters with no immediate relation with a differential operator. As shown by Lele (1992), the compact schemes can be used to construct suitable low-pass filters of various orders. Here, order of a filter has its usual meaning of the rate by which the transfer function tends to one as wavenumber tends to zero (see Lele 1992; Durran 2010). The order of the filter can be selected by the requirements that 1) dissipation is kept minimal for accurate, stable solutions and 2) the desired order of accuracy is not degraded by the action of the filter. Here an eighth-order compact filter (Cook and Cabot 2005), which has been of choice in three-dimensional turbulence simulations, and a sixth-order filter among the family of filters introduced by Lele (1992) have been selected for the present computations. A preliminary assessment of the two filters was carried out for the problem of inertia-gravity wave generation in the two-layer experiments of Mirzaei et al. (2012).

Both qualitative and quantitative results showed that the application of the sixth-order filter to the divergence field provides more reliable estimates of imbalance near the grid scale.

For a discrete field  $F$  with values  $F_j$  in either direction, zonal or meridional, the stencil of the filters has the form

$$\sum_{i=0}^{i=2} b_i (\hat{F}_{j-i} + \hat{F}_{j+i}) = \sum_{i=0}^{i=4} a_i (F_{j-i} + F_{j+i}), \tag{3.10}$$

where  $\hat{F}_j$  is the filtered  $F$  at point  $j$  and the filter coefficients are

$$\begin{aligned} b_0 &= 0.5, 0.5, & b_1 &= 0.666\ 24, 0, & b_2 &= 0.166\ 88, 0.3, \\ 2a_0 &= 0.999\ 65, 0.5, & a_1 &= 0.666\ 52, \frac{3}{8}, & a_2 &= 0.166\ 74, \frac{3}{20}, \\ a_3 &= 4 \times 10^{-5}, \frac{1}{40}, & \text{and} & & a_4 &= -5 \times 10^{-6}, 0, \end{aligned}$$

where for each  $a$  and  $b$ , the two numbers given refer to, respectively, the values for the eighth- and sixth-order filters.

A preliminary assessment of the impact of the filters can be provided by looking at their transfer functions as applied in planar geometry with doubly periodic boundary conditions. According to (3.7), the diffusion operator discretized in time using a backward scheme transforms a two dimensional field  $\eta$  to a field  $\tilde{\eta}$  according to  $\tilde{\eta} = (1 - 2\nu_m \Delta t \nabla^2)^{-1} \eta$ . Analyzing the effect on harmonic solutions  $\eta = e^{i(kx+ly)}$  gives

$$T_D(k, l) = \{1 - 2\nu_m \Delta t [T_2(k) + T_2(l)]\}^{-1}, \tag{3.11}$$

where  $T_D$  is the transfer function defined by  $\tilde{\eta} = T_D \eta$ ,  $i = \sqrt{-1}$ ,  $k$  and  $l$  are the wavenumbers in  $x$  and  $y$  directions, and  $T_2$  is the transfer function for the second derivative (see Esfahanian et al. 2005). For the compact spatial filters (3.10), the transfer function becomes

$$T_F(k, l) = \frac{\sum_{i=0}^{i=4} a_i \cos(kid) \sum_{j=0}^{j=4} a_j \cos(ljd)}{\sum_{i=0}^{i=2} b_i \cos(kid) \sum_{j=0}^{j=2} b_j \cos(ljd)}. \tag{3.12}$$

It can be seen that  $T_F(k_{\max}, l) = T_F(k, l_{\max}) = 0$ , where  $k_{\max} = l_{\max} = \pi/d$ . That is, the filters remove the two-grid-interval wave in each direction for arbitrary wavenumbers in the other direction. This property is not shared by the two-dimensional diffusion operator. Note that while  $T_D$  is explicitly dependent on the time step  $\Delta t$ ,  $T_F$  is independent of  $\Delta t$ . Therefore, to make a meaningful comparison in terms of total wavenumber

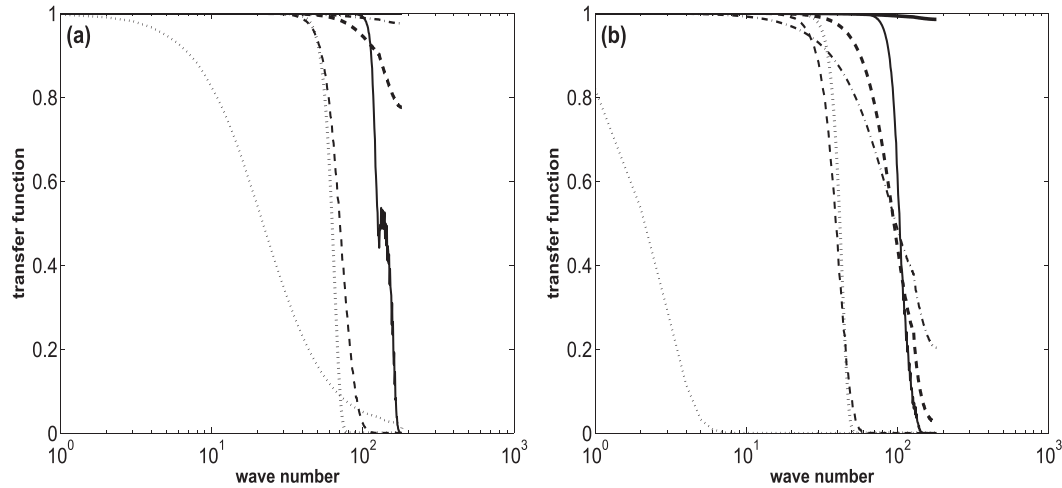


FIG. 1. The one-dimensional transfer function  $T_D$  for (a) one application and (b) 100 applications of the diffusion operator to the second (thick solid line), tenth (dash-dotted), and highest (dotted) vertical modes, as well as the sixth-order (dashed) and the eighth-order (solid) compact filters, the fourth-order hyperdiffusion (thick dashed), and the Broutman filter (thick dotted).

$\kappa = (k^2 + l^2)^{1/2}$ , we have computed the two-dimensional transfer function  $T^{0.1/\Delta t}$  for wavenumbers  $(k, l)d \in ([-\pi, \pi], [-\pi, \pi])$  for a discrete grid with  $k_{\max} = l_{\max} = 256$  and averaged it in circular bands of width  $\Delta\kappa = 1$  to obtain a one-dimensional distribution. To complete the presentation of our filters and provide a point of comparison, also computed are the transfer functions of the Broutman spectral filter used here for dealiasing, and the biharmonic diffusion  $\nu_h \nabla^4$  used in the spectral Eulerian (EUL) dynamical core of the Community Atmosphere Model, version 3 (CAM3), with  $\nu_h = 1.0 \times 10^{15}$  for T85 resolution (Jablonowski and Williamson 2006a) that has 256 grid points in the zonal direction.

Plots of the resulting one-dimensional distributions of the transfer functions are given in Fig. 1. The figure shows that 1) the eighth-order filter is highly scale selective and sharper than the hyperdiffusion of EUL, even after 100 applications; 2) the first baroclinic mode remains intact with the action of the diffusion operator; 3) the sixth-order filter provides higher-scale selectivity than the diffusion acting on the tenth vertical mode; 4) the highest vertical mode is almost entirely eliminated after 100 applications of the diffusion operator. From the figure it is also clear that the dealiasing Broutman and the sixth-order filters share almost the same properties. They act quite close to  $k = 86$ , that is, the cutoff wavenumber of standard de-aliasing in EUL. When compared with EUL, it can be said that the combined effects of the sixth-order and Broutman filters take the place of standard dealiasing and the eighth-order filter takes the place of hyperdiffusion.

### c. Vertical differencing

For the hybrid  $\sigma$ - $\theta$  coordinate, Konor and Arakawa (1997) introduced an energy-conserving vertical differencing scheme using the Charney-Phillips grid, which is adopted here. To use this scheme in our algorithms, we need the vertically discrete form of the hydrostatic equation, the thermodynamic equation, and the vertical mass flux divergence in (2.2) and (3.1). The latter is naturally approximated by  $-[(m\dot{\xi})_{l+1/2} - (m\dot{\xi})_{l-1/2}]/(\delta\xi)_l$  where  $(\delta\xi)_l = \xi_{l+1/2} - \xi_{l-1/2}$  and the mass density  $m$  is equal to  $-(p_{l+1/2} - p_{l-1/2})/(\delta\xi)_l$ . For the hydrostatic equation, as discussed in Konor and Arakawa (1997), one has the option to use any suitable discretization of either  $\partial M/\partial\theta = \Pi$  or  $\partial\Phi/\partial\Pi = -\theta$ . It is also possible to use (2.5). For consistency with energy conservation, we use

$$\begin{aligned} \Phi_l &= \Phi_{l+1} + \theta_l(\Pi_{l+1/2} - \Pi_l) \\ &\quad + \theta_{l+1}(\Pi_{l+1} - \Pi_{l+1/2}) \quad (l = 1, 2, \dots, L-1) \quad \text{and} \end{aligned} \tag{3.13a}$$

$$\Phi_L = \Phi_{L+1/2} + \theta_L(\Pi_{L+1/2} - \Pi_L), \tag{3.13b}$$

where  $\Pi_{L+1/2} = \Pi_s$ . The thermodynamic equation is written as

$$\left(\frac{\partial\theta}{\partial t}\right)_{l+1/2} = -\mathbf{a}_{l+1/2} \cdot \nabla\theta_{l+1/2} - b_{l+1/2}(m\dot{\xi})_{l+1/2}, \tag{3.14}$$

where

$$\mathbf{a}_{l+1/2} = \frac{m_{l+1}\Pi_{l+1}\mathbf{V}_{l+1}(\delta\xi)_{l+1} + m_l\Pi_l\mathbf{V}_l(\delta\xi)_l}{m_{l+1}\Pi_{l+1}(\delta\xi)_{l+1} + m_l\Pi_l(\delta\xi)_l} \quad \text{and}$$

$$b_{l+1/2} = \frac{\Pi_{l+1/2}(\theta_{l+1} - \theta_l)}{\frac{1}{2}[m_{l+1}\Pi_{l+1}(\delta\xi)_{l+1} + m_l\Pi_l(\delta\xi)_l]} \quad (3.15)$$

The full-integer level values of the thermodynamic variables  $\theta_l$  and  $\Pi_l$  are determined from the corresponding half-integer level values by

$$\theta_l = \frac{1}{2}(\theta_{l+1/2} + \theta_{l-1/2}) \quad \text{and} \quad (3.16a)$$

$$\Pi_l = \frac{1}{1 + \kappa} \frac{\Pi_{l+1/2}p_{l+1/2} - \Pi_{l-1/2}p_{l-1/2}}{p_{l+1/2} - p_{l-1/2}} \quad (3.16b)$$

Note that (3.16b) is the finite-difference approximation to the exact relation  $\Pi = [1/(1 + \kappa)]\partial(p\Pi)/\partial p$ . To close the equations, one needs the diagnostic equation for the vertical mass flux  $m\dot{\xi}$ . Taking the time derivative of  $\xi = F(\sigma, \theta)$ , the following equation is obtained:

$$\frac{\partial p}{\partial t} = \frac{p_s - p_{\text{top}}}{\partial F/\partial \sigma} \frac{\partial F}{\partial \theta} \frac{\partial \theta}{\partial t} + (1 - \sigma) \frac{\partial p_s}{\partial t} \quad (3.17)$$

Substituting the time tendencies of  $p$  and  $p_s$  from (2.25) and that of  $\theta$  from (3.14) into (3.17), one arrives at the relation

$$\begin{aligned} & \left[ 1 + b \left( \frac{p_s - p_{\text{top}}}{\partial F/\partial \sigma} \right) \frac{\partial F}{\partial \theta} \right] (m\dot{\xi}) \\ & = -\dot{\omega} + (1 - \sigma) \frac{\partial p_s}{\partial t} - \left( \frac{p_s - p_{\text{top}}}{\partial F/\partial \sigma} \right) \frac{\partial F}{\partial \theta} \mathbf{a} \cdot \nabla \theta, \end{aligned} \quad (3.18)$$

which is used to determine the vertical mass flux at each time step. It is then possible to time step (2.2) at all layers, find  $p$  at all half levels including  $p_s$  using the top boundary condition of  $p' = 0$ , and recover  $\theta$  at each half-integer level using the definition of the vertical coordinate  $\xi = F(\sigma, \theta)$ . In the algorithms developed, in this way no independent time stepping of  $\theta$  is undertaken. The time stepping of  $\theta$  is in fact implicit in the construction of (3.18). At the lower boundary, since  $\xi = f(\sigma)$  the procedure outlined above fails to determine  $\theta$ . Therefore,  $\theta_s$  is taken as a prognostic variable and solved by the same semi-Lagrangian advection method used for  $Q_d$  in CA and  $Q$  in SL.

Finally, for energy conservation, the vertical advection of the velocity components  $u$  and  $v$  at full-integer levels required in (3.1)–(3.3) is evaluated using the scheme proposed by Simmons and Burridge (1981), that is, for  $u$ :

$$\left( \dot{\xi} \frac{\partial u}{\partial \xi} \right)_l = \frac{\left( \dot{\xi} \frac{\partial p}{\partial \xi} \right)_{l+1/2} (u_{l+1} - u_l) + \left( \dot{\xi} \frac{\partial p}{\partial \xi} \right)_{l-1/2} (u_l - u_{l-1})}{2(p_{l+1/2} - p_{l-1/2})} \quad (3.19)$$

with a similar expression for  $v$ .

#### d. Total energy and angular momentum

In the absence of forcing and dissipation, the total energy (Kasahara 1974)

$$E = \int_{AG} \frac{1}{2} \left[ \int_{\xi_{\text{top}}}^{\xi_s} \left( \frac{\mathbf{V} \cdot \mathbf{V}}{2} + c_p T \right) \frac{\partial p}{\partial \xi} d\xi + \Phi_s p_s \right] dA \quad (3.20)$$

and the angular momentum

$$J = \int_A \int_{\xi_{\text{top}}}^{\xi_s} \left( u \frac{\partial p}{\partial \xi} + \Omega_E \cos \phi \frac{\partial p'}{\partial \xi} \right) a \cos \phi d\xi dA \quad (3.21)$$

are conserved. The flow-independent contribution to angular momentum involving the integral of  $a\Omega_E \cos^2 \phi \partial \bar{p} / \partial \xi$  has not been included in  $J$ . The integral invariants  $E$  and  $J$  of the primitive equations in the continuous, conservative limit are used here to monitor the working of the algorithms developed. It should be noted that while the vertical differencing is energy conserving, the other aspects of the algorithms constructed, including spatial discretization and damping procedures, violate conservation of  $E$ . No energy fixer has been applied in the results reported below.

### 4. Results

The setup of the experiments is the test case of Jablonowski and Williamson (2006a) to which readers are referred for details. In brief, using an analytical construction in pressure-based vertical coordinates, the baroclinic/barotropic instability of the zonally symmetric initial state is triggered by the addition of a localized, barotropic perturbation to the wind field. For the hybrid vertical coordinate of Konor and Arakawa (1997) used here in the form  $\xi = f(\sigma) + \theta g(\sigma)$  (see appendix B for details), one has to solve a nonlinear equation at each half-integer level of  $\xi$  to find  $p$  and thus  $\theta$ . In addition to the initial data error stemming from the procedure to solve this nonlinear equation, one has to consider that the interpolation formulae (3.16a) and (3.16b) as well as the discrete hydrostatic equation [(3.13)] may further break the balance of the zonally symmetric part of the initial state. In this regard, one should note that the balanced state of the vertically discrete system in the  $\xi$  coordinate is not the same as that of the vertically continuous system. It should be possible, at least in principle, to determine the balanced zonally symmetric state of the vertically discrete system by using a potential vorticity inversion method. However, the design of a convergent method using Bolin–Charney balance relations (Mohebalhojeh and Dritschel 2001), which are exact for the zonally symmetric jet, seems a formidable

task for the same reasons adumbrated before in the description of the PV-based algorithms using  $\gamma$  or  $P'$  as a prognostic variable. A simpler way is to use a mass inversion, that is, take the thermodynamic fields of  $p$ ,  $\pi$ , and  $\theta$  and determine the vorticity field using the balance relation coming from (3.2) for the zonally symmetric jet,

$$f\zeta = \beta u + \frac{u^2}{a^2} + \frac{1}{a^2 \cos\phi} \frac{d}{d\phi} \left[ \cos\phi \left( \frac{dP'}{d\phi} - \pi' \frac{d\theta'}{d\phi} \right) \right]. \quad (4.1)$$

A similar procedure has been adopted by Skamarock et al. (2012) to reduce small but significant imbalances arising when the analytic expression for the vorticity field is used. Notwithstanding the potential adverse effects of the initial imbalance between the mass and wind fields, in what follows we take the analytic vorticity field to construct the initial state. As it will be shown, with little effects on the baroclinic instability, the initial imbalance mainly impacts the Rossby adjustment process.

For the test case, a selection of results are presented to demonstrate the working and basic properties of the algorithms, which are identified by the parameter  $\alpha$  in (B1) used in the definition of  $g$ , and the parameter  $\tau$  used in (3.9) to determine the strength of vertical-mode-dependent divergence damping. The parameter  $\alpha$  is set to 1 for the slow and 10 for the fast transition from the dominantly  $\sigma$  to the dominantly  $\theta$  vertical coordinate. Results for 26 vertical layers with horizontal resolutions of  $128 \times 128$  and  $256 \times 256$  grid points in longitudinal and latitudinal directions are presented, which are referred to as  $n_g = 128, 256$ , respectively. For numerical stability of the leapfrog time-stepping scheme, the time steps of  $\Delta t = 270, 135$  s are used for, respectively,  $n_g = 128, 256$ . To see this, note that the CFL criterion for the gravity wave equation using the fourth-order compact scheme in the meridional direction demands  $\Delta t \leq (1.732c_{g,\max})^{-1} a \Delta\phi$  [for the stability analysis of the compact scheme, see Lele (1992)], where  $c_{g,\max} \approx 312 \text{ m s}^{-1}$  is the maximum gravity wave speed corresponding to the barotropic mode. From this, the upper limits for the time steps become 289.3, 144.6 s for, respectively,  $n_g = 128, 256$ . The resting basic state is defined based on the global, horizontal mean fields of the zonally symmetric initial state, for which the half-integer values of  $\bar{p}$  are taken from Table B.1 in Jablonowski and Williamson (2006a).

Let us start with the steady-state test case of Jablonowski and Williamson (2006a), which has been designed to test the performance of numerical algorithms in maintaining zonal symmetry. Before presenting the results, a remark on contour representation in spherical coordinates is helpful in understanding the steady-state results. The contour operations involved in

DCASL can be carried out either using the spherical geodesics or the Cartesian longitude–latitude coordinates obtained by a Mercator projection of the sphere. Other transformations can also be envisaged, but these are the two obvious options currently implemented within the codes. Of these two, it is the Cartesian longitude–latitude coordinates that can maintain zonal symmetry. However, in spite of this advantage, numerical experiments show some erroneous distortion of contours during the mature phase of baroclinic instability and appearance of strongly nonzonal flows, apparently coming from an extra degree of smoothing around the contours. For this reason, only results for DCASL with contour operations using spherical geodesics are presented. The consequence is an inevitable breakdown of zonal symmetry and the triggering of baroclinic instability by meridionally propagating inertia–gravity waves generated by the initial imbalance. This is reflected in the results for the norm  $l_2\{[u(t)] - [u(0)]\}$ , defined by

$$\begin{aligned} & \| [u(t)] - [u(0)] \|_2 \\ &= \left( \frac{\sum_k \sum_j \{ [u(t)] - u(0) \}^2 \cos\phi_{i,j} \Delta p_k}{\sum_k \sum_j \cos\phi_{i,j} \Delta p_k} \right)^{1/2}, \quad (4.2) \end{aligned}$$

and shown in Fig. 2. As can be clearly seen, the initial imbalance leads to a rapid deviation of the zonal mean zonal velocity  $[u(t)]$  from its initial value  $[u(0)]$ . This part of the solution up to around time  $t = 15$  is shared by the PS, SL, and CA algorithms used here as well as the CAM Eulerian and finite volume results shown in Fig. 4 of Jablonowski and Williamson (2006a). As expected, at both  $n_g = 128, 256$  resolutions, the initial imbalance is higher for  $\alpha = 10$ . Further, there is a nonconvergence of the  $l_2\{[u(t)] - [u(0)]\}$  with resolution as in the CAM Eulerian results. To explain the nonconvergence, one can note that a significant part of the breakdown of the balance relation (4.1) is due to vertical differencing and thus insensitive to horizontal resolution. The earlier trigger of baroclinic instability of the southern hemispheric jet in the CA solutions, for which evidence will be presented later, is manifest in the slow rise of the error norm during the second part of the simulations. As the  $l_2\{[u(t)] - [u(0)]\}$  measure suffices to demonstrate the general behavior of the DCASL solutions of the steady-state case, the rest of this section examines the baroclinic-wave test case.

To begin with, Fig. 3 presents the surface pressure at day 9 and  $n_g = 128$  resolution for the PS, SL, and CA algorithms with  $\alpha = 1$  (left column) and  $\alpha = 10$  (right column). For the SL and CA algorithms, the vertical-mode-dependent

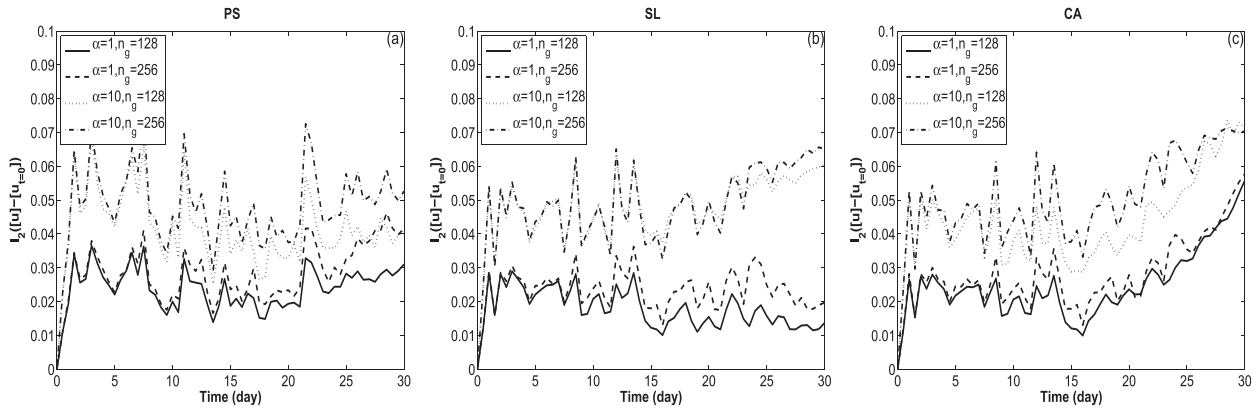


FIG. 2. The  $L_2([u] - [u_0])$  measure for the (a) PS, (b) SL, and (c) CA algorithms with  $\alpha = 1, n_g = 128$  (solid) and  $\alpha = 1, n_g = 256$  (dashed),  $\alpha = 10, n_g = 128$  (dotted) and  $\alpha = 10, n_g = 256$  (dash-dotted).

parameter  $\tau$  is set to 2, 1 days for, respectively,  $\alpha = 1, 10$ . For the PS algorithm, the diffusion coefficient is set independent of vertical mode and so that the damping time for the shortest resolvable wave is 100 days, making the divergence damping virtually ineffective. The reference solutions are given in Figs. 6 and 7 of Jablonowski

and Williamson (2006a). For the main body of the baroclinic wave, that is, the two low-high pairs in the surface pressure with the corresponding feature in the 850-hPa temperature field (not shown), the solutions generally lie between the CAM finite volume solutions at  $2.0^\circ \times 2.5^\circ$  and  $1.0^\circ \times 1.25^\circ$  resolutions. This is particularly the case

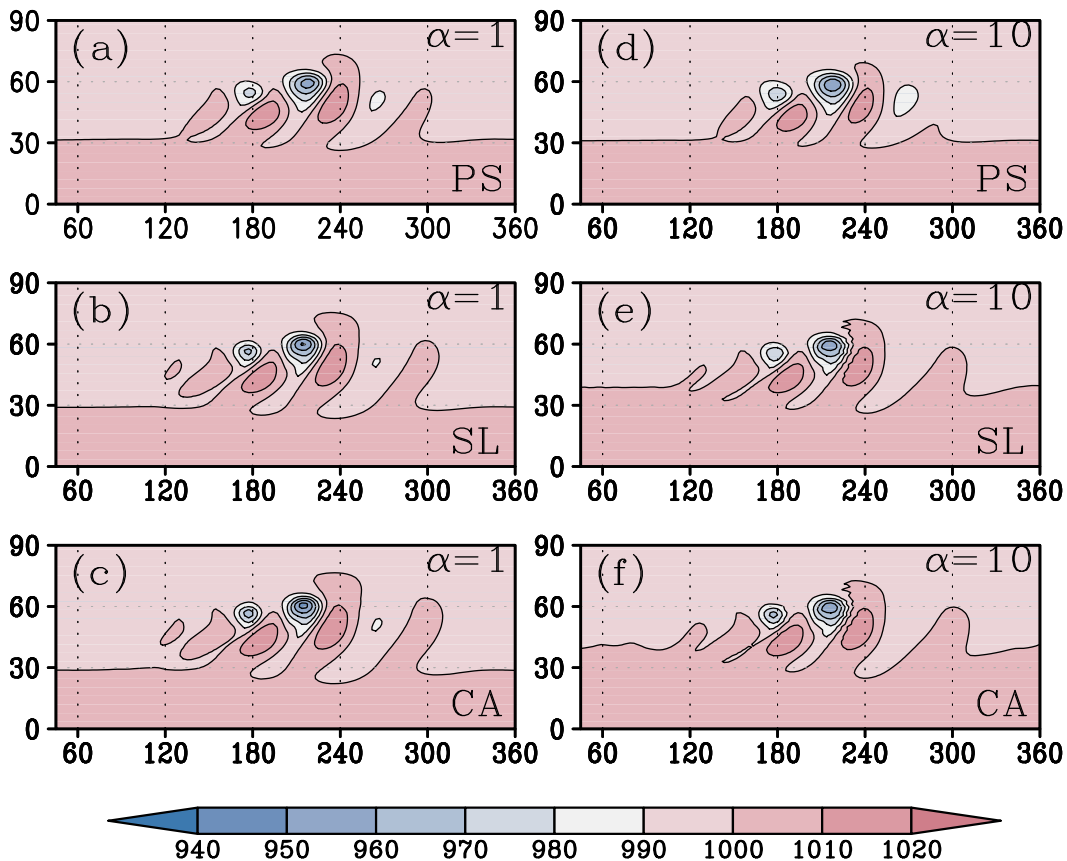


FIG. 3. The surface pressure at day 9 with  $n_g = 128$  for the (a),(d) PS; (b),(e) SL; and (c),(f) CA algorithms for (left)  $\alpha = 1$  and (right)  $\alpha = 10$ .

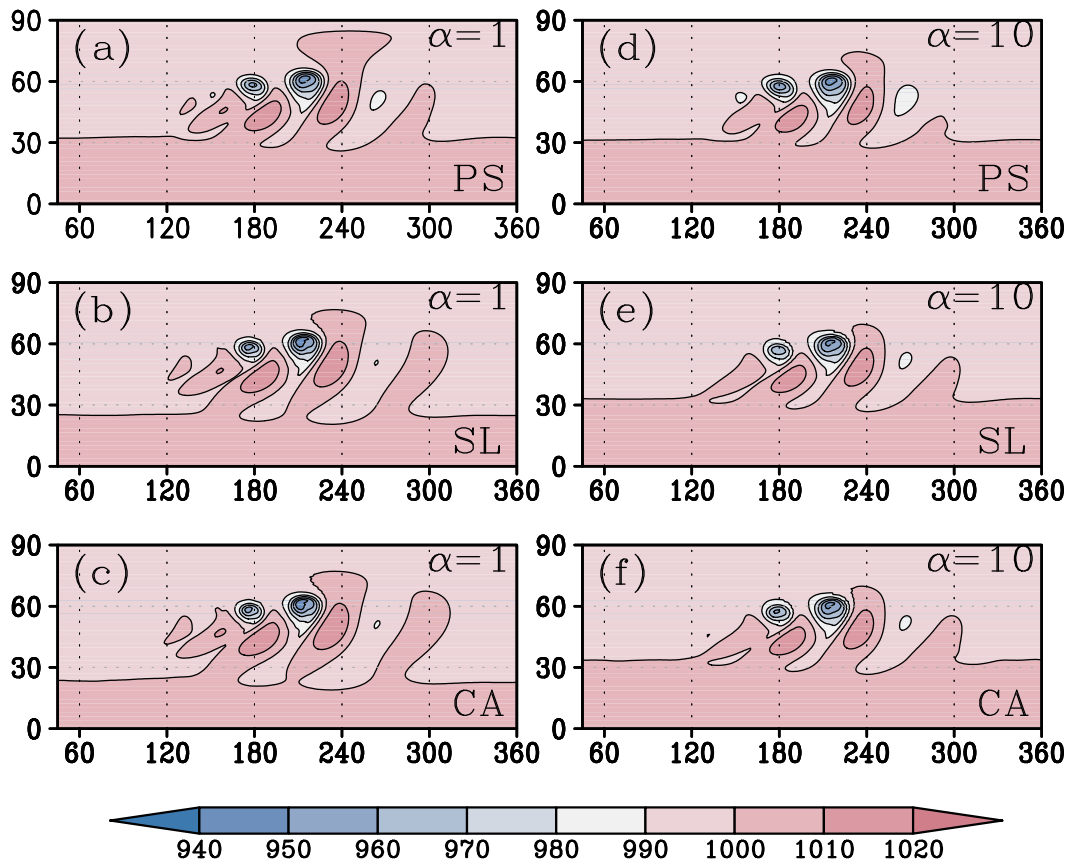


FIG. 4. As in Fig. 3, but for  $n_g = 256$ .

for the CA and SL solutions with  $\alpha = 1$ , which have a stronger surface pressure disturbance than the solution with  $\alpha = 10$ . The main deviation from the reference solutions is in the trailing and leading parts of the wave packet exhibited in the surface pressure field, precisely where there is also a degree of uncertainty in the four reference solutions shown in Fig. 7 of Jablonowski and Williamson (2006a). Compared with the reference solutions, there is also a reverse equator-to-pole pressure gradient that results from the barotropic Rossby adjustment process taking place because of the projection of small imbalance onto the barotropic mode.

The corresponding results for surface pressure at the higher resolution of  $n_g = 256$  are shown in Fig. 4. For the SL and CA algorithms, the vertical-mode-dependent parameter  $\tau$  is set to 0.2, 0.1 days for, respectively,  $\alpha = 1, 10$ . For the PS, the vertically uniform diffusion coefficient is set so that the damping time for the shortest resolvable wave is 10 days. What is most striking is the increase in amplitude of the baroclinic waves, making them closely comparable to the reference solutions. The main differences are again in the trailing and leading parts of the solutions and in the reverse equator-to-pole pressure gradient. To see that the

reverse pressure gradient is indeed a product of the initial imbalance, the corresponding results for the CA algorithms have been presented in Fig. 5 by initializing the zonally symmetric vorticity field using the balance relation (4.1). In this construction, for simplicity, in the right-hand side of (4.1) the analytic zonal velocity has been used, and the smaller nonlinear term due to variation of  $\theta$  on  $\xi$  surfaces has been ignored.

To better understand how the surface pressure amplitude varies with algorithm and resolution, the surface pressure minima and maxima over the domain at  $t = 9$  are given in Table 1. For  $\alpha = 1$ , the picture is clear. The smallest difference between the  $128 \times 128$  and  $256 \times 256$  solutions, the largest maximum, and the smallest minimum all come from the CA algorithm for which the extrema of (942.75, 1018.23) are closely comparable to the CAM Eulerian at T170 resolution, for which the corresponding extrema are (942.62, 1019.33) hPa. For  $\alpha = 10$ , however, the picture is more complex. While the largest maximum comes from the CA algorithm at both resolutions (though with a small margin), the lowest minimum comes from the PS solution. The data for the reference solution of the CAM Eulerian were taken from the Atmospheric Dynamics Modeling Group at the

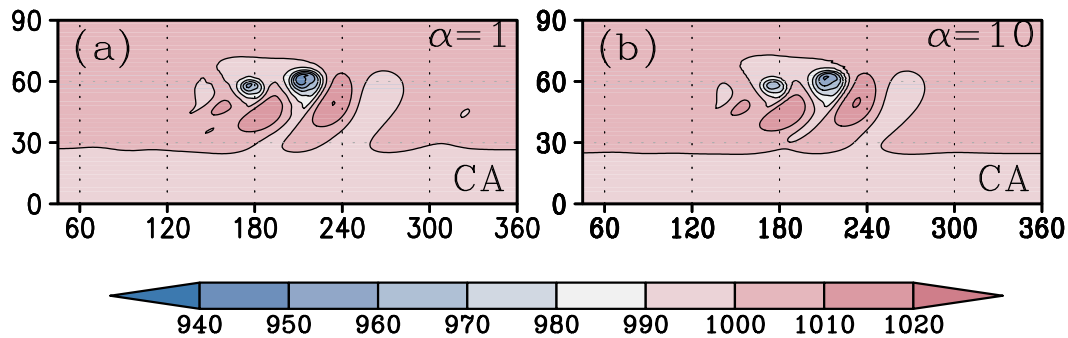


FIG. 5. The surface pressure at day 9 with  $n_g = 256$  for the CA algorithm with (a)  $\alpha = 1$  and (b)  $\alpha = 10$ . The balance relation (4.1) has been used to construct the initial vorticity field.

University of Michigan ([http://clasp-research.engin.umich.edu/groups/admg/ASP\\_Colloquium.php](http://clasp-research.engin.umich.edu/groups/admg/ASP_Colloquium.php)).

Next we turn our attention to the 850-hPa relative-vorticity field at day 9 for which reference solutions have been given in Fig. 8 of Jablonowski and Williamson (2006a). It should be noted that unlike the smoother surface pressure field, there are substantial differences in the finescale structure of the waves among the reference solutions at the peak of instability at  $t = 9$ . Let us see how our algorithms perform at  $n_g = 128$  resolution first (Fig. 6). The increase in amplitude by going from the PS to the SL and to the CA algorithms is evident. The PS solutions are also slightly ahead in phase with respect to the other solutions. Numerical experiments show that this phase shift comes from the action of the larger Robert–Asselin filter in the PS algorithm. Comparing the  $\alpha = 1$  and  $\alpha = 10$  solutions, while there is little effect of the vertical coordinate in the PS algorithm, the higher amplitudes of the  $\alpha = 1$  solutions of the SL and CA algorithms are discernible. Further, the  $\alpha = 10$  solution has a phase lead of a few degrees with respect to the  $\alpha = 1$  solution. Together with the associated reduction in amplitude, the above phase errors are responsible for the higher deviation of the  $\alpha = 10$  solution from the reference solutions. Focusing on the CA solutions, the smaller amplitude of the baroclinic wave in the  $\alpha = 10$  solution is apparent in the two strong positive relative vorticity centers in the  $\alpha = 1$  solution, which itself is generally comparable to the T85 spectral and the  $1.0^\circ \times 1.25^\circ$  finite-volume solutions presented in Jablonowski and Williamson (2006b).

The corresponding solutions obtained using  $n_g = 256$  resolution are shown in Fig. 7. The remarks made on the comparison of the  $\alpha = 1$  and  $\alpha = 10$  solutions at  $n_g = 128$  remain valid. The near doubling of the positive relative vorticity centers make the  $\alpha = 1$  CA solution comparable to the T170 spectral and the  $0.5^\circ \times 0.625^\circ$  finite-volume solutions presented in Jablonowski and Williamson (2006b). To better appreciate the impact of the algorithms, the domain values of minimum and maximum relative vorticity,  $\zeta_{\min}$  and  $\zeta_{\max}$ , respectively, are given in Table 2. Although not so evident at  $t = 9$ , the impact of using contour representation in the CA emerges more clearly where the flow becomes more complex at later times. To demonstrate that, shown in Fig. 8 are the 850-hPa relative-vorticity fields at day 15 for  $\alpha = 1$  CA and SL algorithms. One can also see the earlier trigger of the Southern Hemispheric jet instability in the CA solution, which is a consequence of using the spherical geodesics in contour operations as remarked earlier.

With the visual inspection made in Figs. 3–8 in mind, let us turn to some quantitative measures of the working of the PS, SL, and CA algorithms. The first measure is the  $l_2$  norm of the difference between the solutions obtained by these algorithms and the reference solutions for the surface pressure defined by

$$\|p_s - p_{s,\text{ref}}\|_2 = \left[ \frac{\sum_i \sum_j (p_s - p_{s,\text{ref}})^2 \cos\varphi_{ij}}{\sum_i \sum_j \cos\varphi_{ij}} \right]^{1/2}, \quad (4.3)$$

TABLE 1. The extrema of surface pressure (hPa) at  $t = 9$ . In each column, the first and second numbers are, respectively, for minimum and maximum values of surface pressure over the sphere.

Resolution	PS – 1	PS – 10	SL – 1	SL – 10	CA – 1	CA – 10
$128 \times 128$	955.33, 1016.80	951.65, 1015.31	948.68, 1016.86	952.68, 1016.27	946.29, 1017.52	951.23, 1017.00
$256 \times 256$	945.07, 1016.95	944.72, 1015.20	943.41, 1017.93	945.46, 1016.07	942.75, 1018.23	946.65, 1016.16

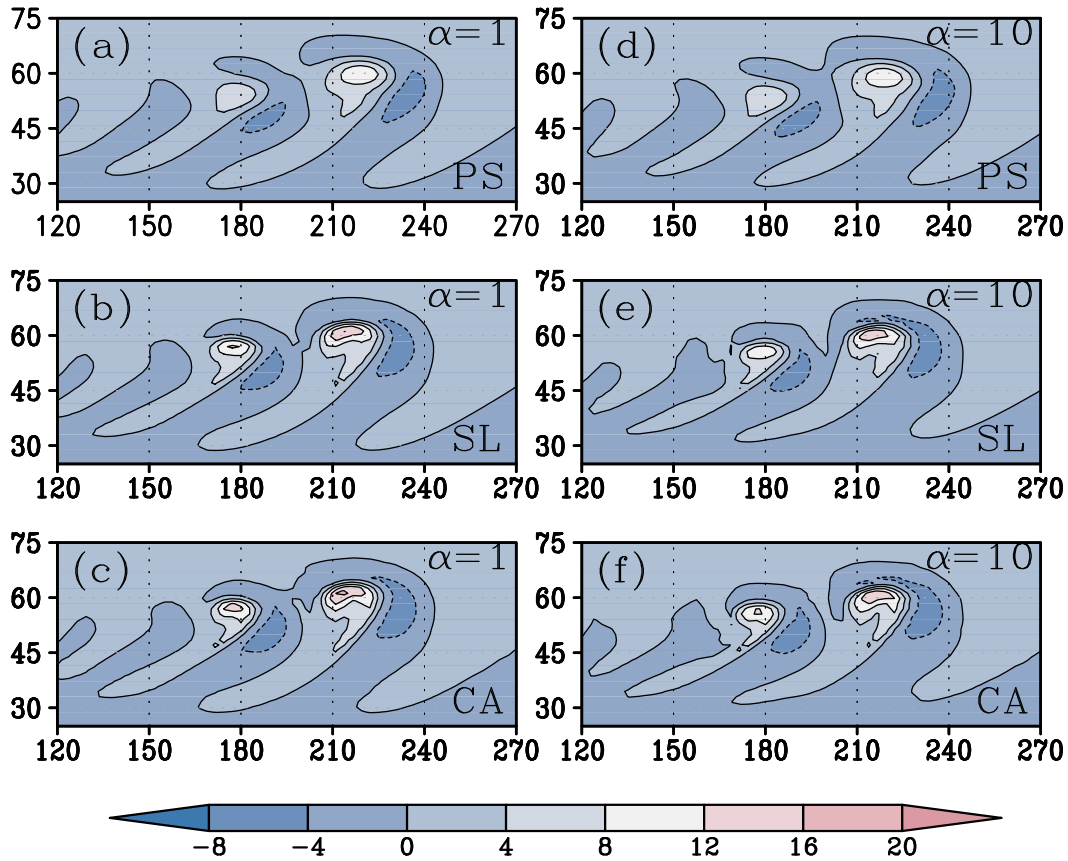


FIG. 6. The relative vorticity field at day 9 with  $n_g = 128$  for the (a),(d) PS; (b),(e) SL; and (c),(f) CA algorithms for (left)  $\alpha = 1$  and (right)  $\alpha = 10$ .

where the sums are taken over all points of the half-grid used in the algorithms designed. The half-grid refers to a grid shifted by a half-grid interval in the meridional direction with respect to the poles. To determine (4.3), the reference solution is first interpolated to the half-grid using a fourth-order cubic Hermite interpolation. Using (4.3),  $\|p_s^* - p_{s,\text{ref}}^*\|_2$  has also been computed, where  $p_s^*$  denotes the deviation of the surface pressure from the zonal average. This is useful, as  $\|p_s - p_{s,\text{ref}}\|_2$  is largely contaminated by the meridional noise arising from initialization errors. The results of the PS, SL, and CA algorithms at  $n_g = 256$  resolution are presented in Fig. 9, where the reference solution is the spectral Eulerian solution at T170 resolution. When compared with the model intercomparison shown in Fig. 10 of Jablonowski and Williamson (2006a), until the buildup of baroclinic instability, the pressure difference between the solutions obtained and the reference solutions is more than an order of magnitude larger than the cross-model differences in Jablonowski and Williamson (2006a). However, when the contribution of the zonally averaged part of the solution is removed in  $\|p_s^* - p_{s,\text{ref}}^*\|_2$ , the difference

field shown in Fig. 9b becomes close to the cross-model differences. Among the solutions shown, during the first 15 days of the simulation, the closest and furthest results to the reference solution come from, respectively, the CA algorithm with  $\alpha = 1$  and the PS algorithm with  $\alpha = 10$ . For each of the PS, SL, and CA algorithms, the pressure differences are larger for  $\alpha = 10$ . This observation is related to the fact that the use of  $\alpha = 10$  leads to a larger initial imbalance.

An examination of total energy [(3.20)] and angular momentum [(3.21)] gives us further information on the global conservation properties of the algorithms. Figure 10 shows the percentage relative changes in total energy,  $\{[E(t) - E(0)]/E(0)\} \times 100$  and angular momentum at  $n_g = 128, 256$  resolutions. Overall, a wide range of behavior is exhibited by the algorithms for the time variation in energy and angular momentum. At both resolutions, the two PS algorithms dissipate energy and angular momentum with a slightly higher rate for  $\alpha = 10$ . For the SL algorithms, the buildup of energy during the 30-day integrations is considerably lower at  $n_g = 256$  resolution. Regarding angular momentum, except

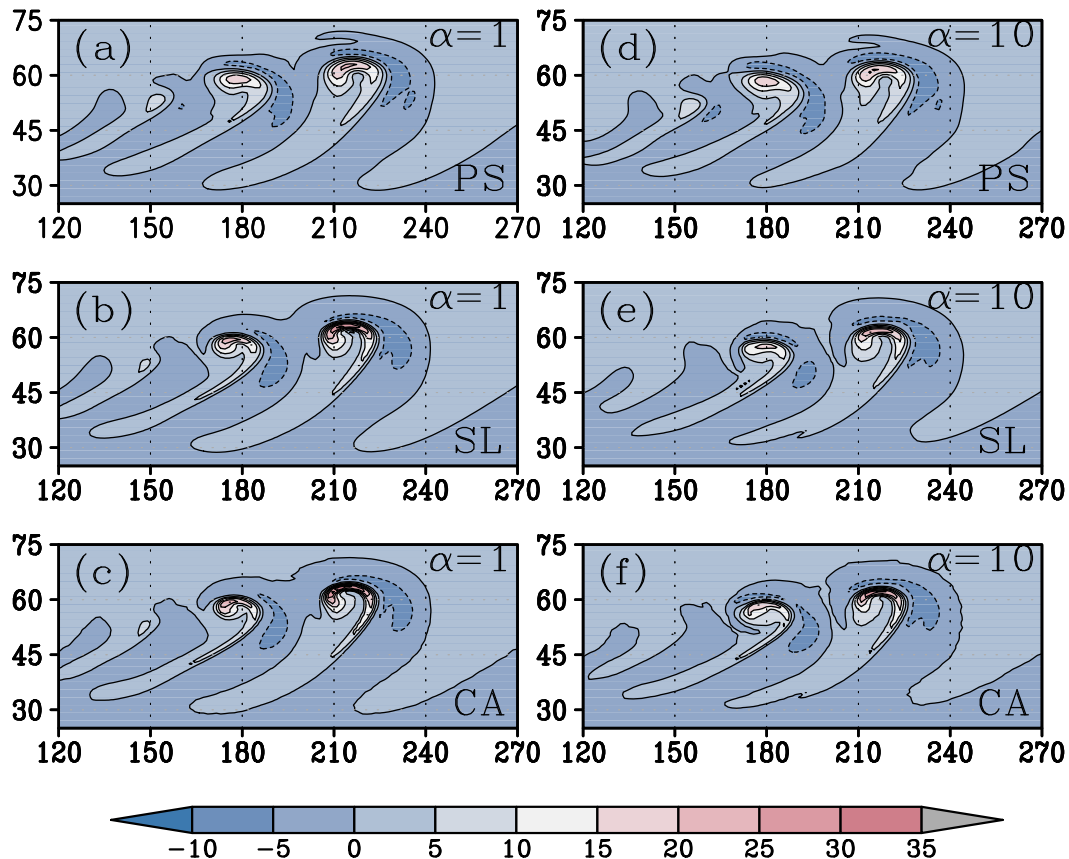


FIG. 7. As in Fig. 6, but for  $n_g = 256$ .

for the generally increasing behavior seen for  $\alpha = 1$  at  $n_g = 128$  resolution, the remaining SL algorithms exhibit oscillatory results. At both resolutions and for both vertical coordinates, the CA results are indistinguishable from the corresponding SL results over the first 12–14 days of integration, that is, within the range of predictability of the flow (see Jablonowski and Williamson 2006a). Beyond around time  $t = 14$ , the CA results diverge strongly from the corresponding SL results, particularly so for energy at  $\alpha = 10$  and angular momentum at  $\alpha = 1$ . It should be noted that at  $n_g = 256$  resolution, for  $\alpha = 10$  the application of the eighth-order filter in the zonal direction results in a substantial buildup of small-scale noise around the equator, leading to numerical instability during the second-half of the simulations. For this reason, the SL and CA results

for  $\alpha = 10$  shown here have been obtained by applying the eighth-order filter only in meridional direction to the  $\bar{h}$  field.

The relative changes in energy seen in Fig. 10 may seem excessive. In the absence of results to compare to in the literature, we resort to indirect comparisons. First, a basic comparison can be made with the results presented in Fig. 4 of Mohebalhojeh and Dritschel (2007) documenting the variations in energy for various CASL algorithms applied to the test case of Galewsky et al. (2004) for the spherical SW equations. The relative changes are well within the range of values seen in that test case. Second, another possible point of comparison is the  $0.6 \text{ W m}^{-2}$  estimate given in Taylor (2011) for the dissipation rate of kinetic energy, which is the main contributing factor to energy dissipation in aquaplanet

TABLE 2. The extrema of relative vorticity ( $\text{day}^{-1}$ ) at  $t = 9$ . In each column, the first and second numbers are, respectively, for minimum and maximum values of  $\zeta$  over the sphere.

Resolution	PS - 1	PS - 10	SL - 1	SL - 10	CA - 1	CA - 10
$128 \times 128$	-6.10, 11.75	-6.21, 11.16	-5.63, 16.25	-5.86, 14.71	-5.88, 17.12	-5.80, 16.25
$256 \times 256$	-8.36, 20.84	-8.62, 20.45	-6.51, 32.50	-7.04, 26.37	-7.04, 36.30	-6.87, 29.37

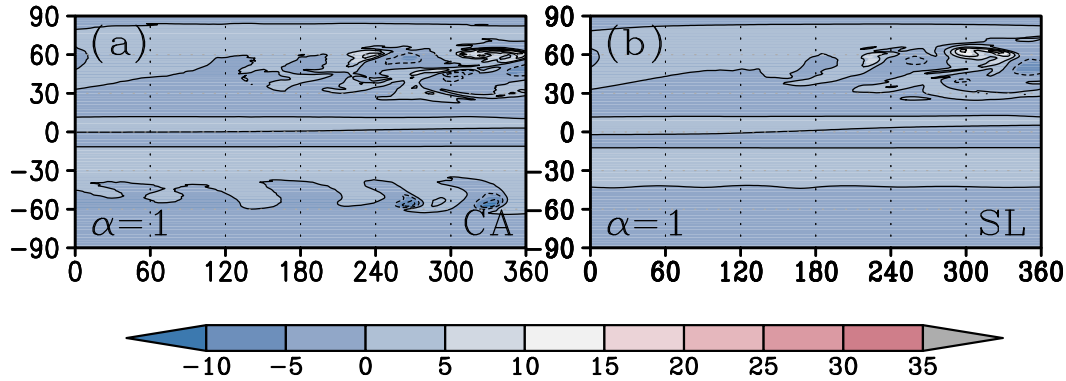


FIG. 8. The relative vorticity field at day 15 with  $n_g = 256$  and  $\alpha = 1$  for (a) the CA and (b) the SL algorithms.

simulations by the CAM–High-Order Method Modeling Environment (HOMME) model (Neale et al. 2012). To demonstrate the effect of overusing divergence damping (an extreme case of energy dissipation), also shown in Fig. 10c is the result for the CA algorithm with  $\alpha = 10$  with a doubling of the vertical-mode-dependent damping. In this strongly dissipative case, we have  $E(t=0) = 1.3127 \times 10^9 \text{ J m}^{-2}$ ,  $E(t=30) = 1.3114 \times 10^9 \text{ J m}^{-2}$ , and  $[E(t=30) - E(t=0)]/(30 \text{ days}) = -0.5 \text{ W m}^{-2}$  as a rough estimate for the average energy dissipation rate over the 30 days of integration. It is true that the instantaneous picture is much more complex, where bursts of dissipation may be followed by larger periods of conservation. But overall, the average dissipation rate over sufficiently large time intervals can be expected to fall not far from the  $0.6 \text{ W m}^{-2}$  estimate of Taylor (2011).

A further comparison can be made by quantifying the relative strength of the vortical flow in the CA solution with that in the PS and SL solutions. To this end, first the quantities  $C_2$  and  $D$  defined per unit area as

$$C_2 = \frac{1}{2} \langle (1 + \tilde{h}) \tilde{\zeta}^2 \rangle \quad \text{and} \quad (4.4a)$$

$$D = \frac{1}{2} \langle (1 + \tilde{h}) |\nabla \tilde{\zeta}| \rangle \quad (4.4b)$$

are computed for each 30-day integration. Here  $\langle \rangle$  denotes the domain-area average over the Northern Hemisphere. Because of the earlier trigger of the southern hemispheric jet instability in the CA solution (Fig. 8), for a better assessment, the Southern Hemisphere has been excluded from the averaging. Taking the CA results at each resolution as the reference, the relative differences, like  $[C_2(\text{SL}) - C_2(\text{CA})]/C_2(\text{CA})$  for  $C_2$  and SL, are then computed. The results with  $\alpha = 1$  are shown in Fig. 11. In both the  $C_2$  and  $D$  measures, the substantial reduction seen for the PS algorithm points to a dramatic underestimation of vortical activity with respect to CA. The overshoot in  $D$  seen over the first 5 days of integration comes from a stronger generation of meridional imbalance in the PS solution. The SL

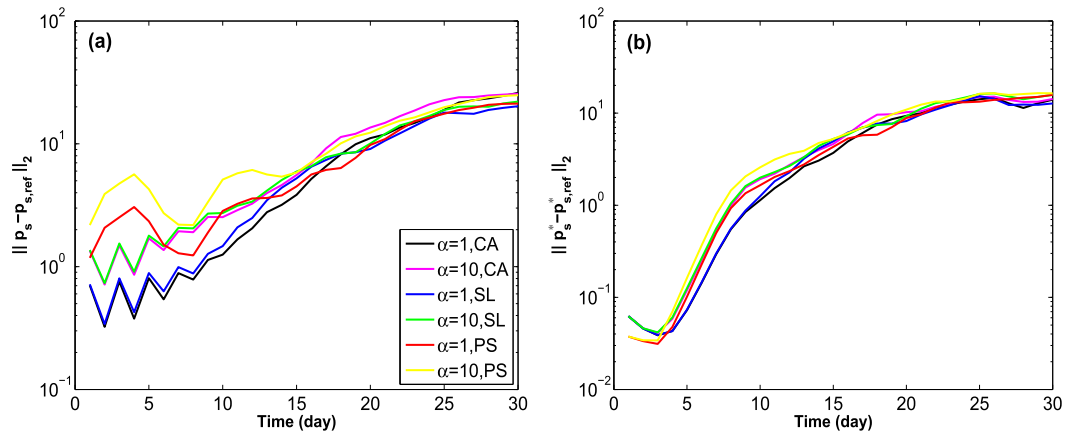


FIG. 9. The quantitative measures of departure from the reference solution, taken to be that of the T170 Eulerian spectral model, for  $n_g = 256$ : (a)  $\|p_s - p_{s,\text{ref}}\|_2$  and (b)  $\|p_s^* - p_{s,\text{ref}}^*\|_2$  for the PS algorithm with  $\alpha = 1$  (red) and  $\alpha = 10$  (yellow), the SL algorithm with  $\alpha = 1$  (blue) and  $\alpha = 10$  (green), and the CA algorithm with  $\alpha = 1$  (black) and  $\alpha = 10$  (magenta).

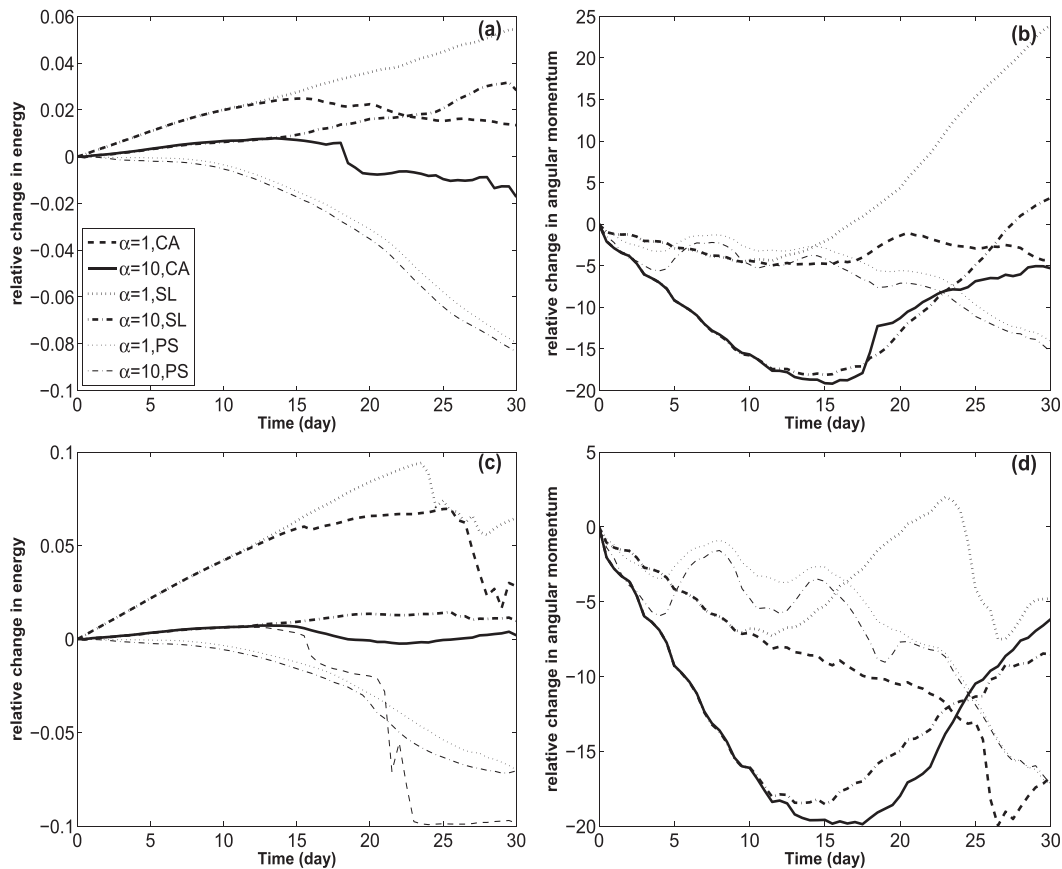


FIG. 10. The percentage relative changes in total energy and angular momentum for (a),(b)  $n_g = 128$  and (c),(d)  $n_g = 256$ . The results shown are for the PS algorithm with  $\alpha = 1$  (thin dotted) and  $\alpha = 10$  (thin dash-dotted), the SL algorithm with  $\alpha = 1$  (thick dotted) and  $\alpha = 10$  (thick dash-dotted), and the CA algorithm with  $\alpha = 1$  (dashed) and  $\alpha = 10$  (solid). Also shown in (c) is the thin dashed line presenting the result for the CA algorithm with  $\alpha = 10$  but a doubled diffusion coefficient ( $\tau = 0.05$  days).

solution also suffers from a reduction of vortical activity, which is weaker than in the PS solution. There seems to be an exception to this statement because of the peak seen at  $n_g = 256$  around time  $t = 24$ . However, this arises from the fact that vanishing layer thickness with a consequent generation of localized, large values of vorticity occur earlier in the SL solution.

Let us finally examine how the algorithms behave in terms of their kinetic energy spectrum at 700 hPa and  $t = 30$ , for which results are available for the CAM finite volume dynamical core in Jablonowski and Williamson (2011). For  $n_g = 256$  resolution, spectra for the various algorithms are presented in Fig. 12. The main objective here is to highlight the effects of the varying damping procedures employed by the algorithms. The spectral slope between the total wavenumbers 10 and 100 is particularly sensitive to the degree of damping used for regularization of the flow and for numerical stability. The slope in the latter part of the spectrum can be compared with the reference  $n^{-3}$  distribution (Skamarock

2011). This slope is closest to  $n^{-3}$  for the CA algorithm with  $\alpha = 1$ . Further, for each of the PS, SL, and CA algorithms, steeper slopes occur for  $\alpha = 10$ . At the larger-scale end of the spectrum between the total wavenumbers 1 and 10, there is a significant scatter among the results in Fig. 12 as well as those in Jablonowski and Williamson (2011) for the CAM finite volume dynamical core. The scatter seen is much larger with  $\alpha = 10$ . It is interesting to note that at this part of the spectrum, results close to the CAM finite volume dynamical core can be obtained, if the CA algorithm uses solely the sixth-order filter.

#### Computational cost

As an estimate of computational efficiency, the computational cost of the PS, SL, and CA algorithms are given in Table 3, relative to that of the low-resolution PS. Unlike the PS and SL algorithms, the computational cost of CA is heavily dependent on flow complexity. As the complexity substantially increases during the second half of integration, the relative costs have been given for

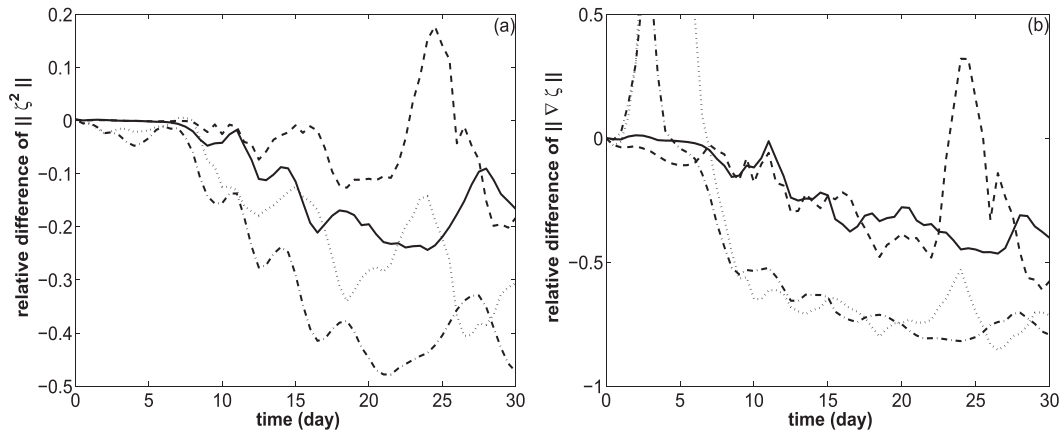


FIG. 11. The relative differences in (a)  $\|\zeta^2\|_2$  and (b)  $\|\nabla\zeta\|_2$  between the solutions of the PS and the DCASL algorithms at  $128 \times 128$  (dash-dotted) and  $256 \times 256$  (dotted) resolutions. Also shown are the relative differences between the solutions of the SL and the DCASL algorithms at  $128 \times 128$  (solid) and  $256 \times 256$  (dashed) resolutions. The results are for  $\alpha = 1$ .

the time intervals  $[0, 15]$  and  $[0, 30]$  days. When compared with the SL algorithm, the computational overhead of incorporating Lagrangian information in the CA algorithm is slight over the  $[0, 15]$  interval, but more than doubles over the  $[0, 30]$  interval. The latter substantial increase comes from the finescale structures that are represented in CA and lost in SL. The impact of such structures, though not so evident in the quantitative measures presented, is expected to be greater in flows more complex than exhibited by the current test case.

**5. Conclusions**

The DCASL algorithms previously developed for the shallow-water equations and the hydrostatic Boussinesq equations have been extended to solve the spherical

hydrostatic primitive equations using a hybrid  $\sigma$ - $\theta$  vertical coordinate. To this end, vertical modes have been formulated for the generalized coordinate by introducing a variable called modified pressure  $P'$  that forms the linear part of the pressure gradient force. The DCASL algorithms solve the primitive equations in any of the  $(Q, \delta, \gamma)$ ,  $(Q, \delta, P')$ ,  $(Q, \tilde{h}, \delta)$  representations where  $Q \equiv (f + \zeta)/(1 + h)$  is a PV-like quantity and  $\gamma \equiv f\zeta - \nabla^2 P' - \beta u$  is an approximation to the horizontal acceleration divergence ( $\nabla \cdot D_h \mathbf{V}/Dt$ ). The deviations of  $Q$  from the Rossby-Ertel PV and  $\gamma$  from horizontal acceleration divergence result from the deviation of the vertical coordinate from an isentropic one. Sufficiently far away from the lower boundary, as  $\xi$  tends to  $\theta$ ,  $Q$  becomes a close approximation to PV and thus the algorithm can be regarded as being PV based. The

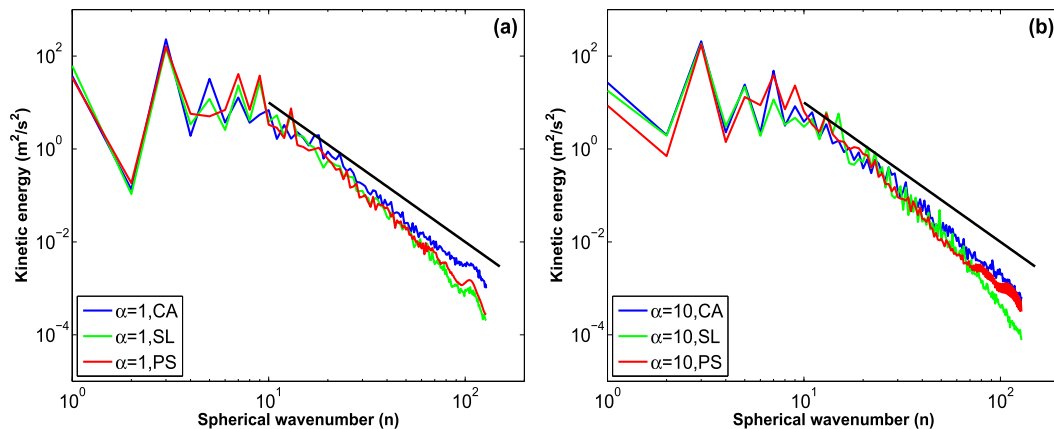


FIG. 12. The kinetic energy spectra at day 30 and at 700 hPa for the PS (red), SL (green), and CA (blue) algorithms with (a)  $\alpha = 1$  and (b)  $\alpha = 10$ . The resolution is  $n_g = 256$ . The straight solid line gives the theoretical  $n^{-3}$  spectrum (see text).

TABLE 3. CPU time relative to the PS simulation at  $128 \times 128$  resolution. In each column, the first and second numbers are, respectively, for the first 15 and 30 days of the experiments.

Resolution	PS – 1	PS – 10	SL – 1	SL – 10	CA – 1	CA – 10
$128 \times 128$	1, 1	0.99, 0.98	1.59, 1.58	1.65, 1.64	2.07, 3.70	2.01, 3.53
$256 \times 256$	9.01, 8.81	8.91, 8.81	13.49, 13.38	12.99, 13.03	13.53, 27.05	15.89, 26.15

algorithm with the prognostic variables  $(Q, \delta, \gamma)$  involves an inversion problem to determine the depth and the thermodynamic fields. The inversion problem, however, turns out to be particularly difficult primarily because of the nonlinearity of the hydrostatic equation in the  $\sigma$ - $\theta$  coordinate used. Except for theoretical models with a few layers, the resulting algorithm appears to be impractical. For the less demanding  $(Q, \delta, P')$  algorithm, which is suitable for applying a semi-implicit scheme, an efficient and convergent method to determine thermodynamic fields from  $P'$  has yet to be found. Therefore, for realistic models with a large number of layers, the focus has been on the  $(Q, \tilde{h}, \delta)$  algorithm with an explicit time-stepping scheme. In addition to the problems with computational cost due to limitation to a short time step, it also turned out that the increased Lagrangian resolution on  $Q$  requires various types of damping, filtering, and regularization for computational stability.

Using the  $(Q, \tilde{h}, \delta)$  algorithm, extensive numerical simulations have been carried out for the test case of baroclinic instability introduced by Jablonowski and Williamson (2006a). This is in fact a stringent test case for the DCASL algorithms developed, because the instability acts strongly at low levels near to the ground where  $\xi$  deviates from  $\theta$ , and thus there are large sources of  $Q$  coming mainly from vertical advection. The numerical assessment of the DCASL algorithm was undertaken together with two other algorithms derived from it: 1) the one called SL replacing the DCASL solution for  $Q$  by a standard semi-Lagrangian solution, and 2) an Eulerian algorithm called PS replacing  $Q$  by  $\zeta$  as the prognostic variable. Various degrees of improvement from modest to significant over the SL and PS solutions at equal grid resolution were demonstrated. At medium horizontal resolutions, the DCASL algorithm can achieve results comparable to the reference solutions shown in Jablonowski and Williamson (2006a,b).

To address the convergence issue with the semi-implicit time-stepping scheme referred to above, work is under way on a modified algorithm that replaces  $P'$  by  $P'_l$ , where  $P'_l$  is obtained by linearizing the right-hand side of (2.5), that is,

$$\frac{\partial P'_l}{\partial \xi} = \Pi' \frac{\partial \bar{\theta}}{\partial \xi} - \theta' \frac{\partial \bar{\Pi}}{\partial \xi}. \quad (5.1)$$

With this change, it is possible to replace the column-wise iterative procedure (A3) by a procedure to solve a nonlinear equation separately for each layer from the bottom to the top of the model.

As a final remark, the need for various types of damping may be seen as the main deficiency of our working DCASL algorithm. To a certain extent, the problem with damping is related to the failure of our device to apply implicitly a form of balance relation, as in the  $(Q, \delta, \gamma)$  algorithm, to control fictitious generation of imbalance. Within the  $(Q, \tilde{h}, \delta)$  algorithm, it seems that other methods to enhance the solution of the mass and divergence fields have to be found. This remains for future development of the basic DCASL algorithm presented here.

*Acknowledgments.* A.R.M. thanks the U.K. Natural Environment Research Council for a Research Fellowship, and the Universities of St. Andrews and Tehran for providing support during this research. Further financial support was provided by IR of Iran Meteorological Organization to which we are thankful. Special thanks also go to Sarmad Ghader, Mohammad Mirzaei, and Daniel Yazgi for their help in preparing the paper.

## APPENDIX A

### Procedure to Invert $Q, \delta$ , and $\gamma$

When the variables  $Q, \delta$ , and  $\gamma$  are used as the prognostic variables, one has to implement an inversion procedure to obtain the velocity field and the thermodynamic variables at each time step. Rewriting the definition of  $\gamma$  as  $\nabla^2 P' = f\zeta - \beta u - \gamma$ , subtracting  $f^2 h$  from both sides, projecting onto the vertical-mode space, and dividing the result by  $c_m^2$ , the following modified Helmholtz equation is obtained:

$$\left( \nabla^2 - \frac{f^2}{c_m^2} \right) \tilde{h} = \frac{1}{c_m^2} \left[ \overbrace{f(\zeta - fh) - \beta u - \gamma}^{\sim} \right]. \quad (A1)$$

It should be noted that the variable  $h$  defined by  $\mathbf{h} = \mathbf{C}^{-1} \mathbf{P}$  is generally different from  $\tilde{h}$ . Equation (A1) is solved using the same method described in Mohebalhojeh and Dritschel (2007) by spectral transform in longitude and

fourth-order compact differencing in latitude. The result for  $h$  leads to the solution for  $P'$  using either of the relations  $\mathbf{P}' = \mathbf{C}\mathbf{h}$  or  $\tilde{P}' = c_m^2 \tilde{h}$ . The task is then to find the thermodynamic variables using the information on  $P'$  in each fluid column. Substituting the relation  $c_p T' = \Pi\theta - \bar{\Pi}\bar{\theta}$  in the definition of  $P'$ , it is easy to obtain

$$P' = \Phi' + \Pi'\theta. \tag{A2}$$

The hydrostatic relation  $\partial\Phi/\partial\Pi = -\theta$  is discretized as in (3.13). Substituting (3.13) in (A2) for  $l = 1, \dots, L$ , and writing the result as a matrix equation for  $(\Pi_{3/2}, \dots, \Pi_{L+1/2})$ , the following iterative solution procedure can be envisaged:

$$\Phi_L^{(k+1)} = \Phi_{L+1/2} + \theta_L^{(k)}(\Pi_{L+1/2}^{(k)} - \Pi_L^{(k)}), \tag{A3a}$$

$$\Pi_L^{(k+1)} = \bar{\Pi}_L + \frac{P'_L - \Phi_L^{(k+1)} + \bar{\Phi}_L}{\theta_L^{(k)}}, \tag{A3b}$$

$$\begin{aligned} \Phi_l^{(k+1)} &= \Phi_{l+1}^{(k+1)} + \theta_l^{(k)}(\Pi_{l+1/2}^{(k)} - \Pi_l^{(k)}) \\ &\quad + \theta_{l+1}^{(k)}(\Pi_{l+1}^{(k+1)} - \Pi_{l+1/2}^{(k)}) \quad (l = L-1, \dots, 1), \text{ and} \end{aligned} \tag{A3c}$$

$$\Pi_l^{(k+1)} = \bar{\Pi}_l + \frac{P'_l - \Phi_l^{(k+1)} + \bar{\Phi}_l}{\theta_l^{(k)}} \quad (l = L-1, \dots, 1), \tag{A3d}$$

where the superscript  $(k)$  refers to the  $k$ th iteration. Having obtained the full-integer values of  $\Pi^{(k+1)}$ , one then can estimate the half-integer values of  $p^{(k+1)}$  and  $\Pi^{(k+1)}$  by solving the nonlinear equation coming from the interpolation relation (3.16b). Another iterative algorithm can also be envisaged by applying the finite-difference approximation of the form of the hydrostatic equation in (2.5) to solve first for the  $\Pi$  values at half-integer levels, including the surface level, and then use (3.16b) to find the full-integer values.

## APPENDIX B

### Construction of the Generalized Vertical Coordinate

The way  $\xi$  is defined as a function of  $\sigma$  and  $\theta$  closely follows Konor and Arakawa (1997). Setting  $\xi = f(\sigma) + g(\sigma)\theta$ , defining  $\sigma$  as an increasing function of height varying from 0 at the surface to 1 at the top level, the functions  $f$  and  $g$  are determined in such a way that 1)  $\xi$  tends to  $\sigma_s$  and  $\theta$  when  $p$  tends to  $p_s$  and  $p_{\text{top}}$ , respectively, and 2) the condition  $\partial\xi/\partial\sigma > 0$  is satisfied to ensure monotonicity whenever  $\partial\sigma/\partial\theta > (\partial\sigma/\partial\theta)_{\text{min}}$  and  $\theta > \theta_{\text{min}}$ . Here  $\theta_{\text{min}}$  and  $(\partial\sigma/\partial\theta)_{\text{min}}$  are prescribed values of the lowest value of potential temperature and the

vertical gradient of potential temperature with respect to  $\sigma$ , respectively. To this end, setting

$$g(\sigma) = \frac{1 - e^{-\alpha\sigma}}{1 - e^{-\alpha}}, \tag{B1}$$

with the desirable properties of  $g(0) = 0$ ,  $g(1) = 1$ , and  $g$  increasing monotonically with height, the function  $f(\sigma)$  is determined by solving the equation

$$\frac{df}{d\sigma} + \theta_{\text{min}} \frac{dg}{d\sigma} + g(\partial\sigma/\partial\theta)_{\text{min}} = 0, \tag{B2}$$

using the upper boundary condition  $f(1) = 0$ . The results for  $f(\sigma)$  and the partial derivative of  $\xi$  with respect to  $\sigma$  required for the computation of  $\xi$  become

$$\begin{aligned} f(\sigma) &= \frac{1}{1 - e^{-\alpha}} \left\{ (e^{-\alpha} - e^{-\alpha\sigma}) \left[ \frac{(\partial\sigma/\partial\theta)_{\text{min}}}{\alpha} - \theta_{\text{min}} \right] \right. \\ &\quad \left. - (\partial\sigma/\partial\theta)_{\text{min}}(\sigma - 1) \right\} \quad \text{and} \end{aligned} \tag{B3a}$$

$$\frac{\partial\xi}{\partial\sigma} = \frac{1}{1 - e^{-\alpha}} \left[ (\theta - \theta_{\text{min}})\alpha e^{-\alpha\sigma} - (1 - e^{-\alpha})(\partial\sigma/\partial\theta)_{\text{min}} \right]. \tag{B3b}$$

## REFERENCES

Akmaev, R. A., 1991: A direct algorithm for convective adjustment of the vertical temperature profile for an arbitrary critical lapse rate. *Mon. Wea. Rev.*, **119**, 2499–2504, doi:10.1175/1520-0493(1991)119<2499:ADAFCA>2.0.CO;2.

Arakawa, A., C. R. Mechoso, and C. S. Konor, 1992: An isentropic vertical coordinate model: Design and application to atmospheric frontogenesis studies. *Meteor. Atmos. Phys.*, **50**, 31–45, doi:10.1007/BF01025503.

Bates, J. R., Y. Li, A. Brandt, S. F. McCormick, and J. Ruge, 1995: A global shallow-water numerical model based on the semi-Lagrangian advection of potential vorticity. *Quart. J. Roy. Meteor. Soc.*, **121**, 1981–2005, doi:10.1002/qj.49712152810.

Bleck, R., 1984: An isentropic coordinate model suitable for lee cyclogenesis simulation. *Riv. Meteor. Aeronaut.*, **43**, 189–194.

—, S. Benjamin, J. Lee, and A. E. MacDonald, 2010: On the use of an adaptive, hybrid-isentropic vertical coordinate in global atmospheric modeling. *Mon. Wea. Rev.*, **138**, 2188–2210, doi:10.1175/2009MWR3103.1.

Charney, J. G., 1962: Integration of the primitive and balance equations. *Proc. Int. Symp. on Numerical Weather Prediction*, Tokyo, Japan, Meteorological Society of Japan, 131–152.

Cook, A. W., and W. H. Cabot, 2005: Hyperviscosity for shock-turbulence interactions. *J. Comput. Phys.*, **203**, 379–385, doi:10.1016/j.jcp.2004.09.011.

Dritschel, D. G., 1988: Contour surgery: A topological reconnection scheme for extended integrations using contour dynamics. *J. Comput. Phys.*, **77**, 240–266, doi:10.1016/0021-9991(88)90165-9.

—, 1989: Contour dynamics and contour surgery: Numerical algorithms for extended, high-resolution modelling of vortex dynamics in two-dimensional, inviscid, incompressible flows. *Comput. Phys. Rep.*, **10**, 77–146, doi:10.1016/0167-7977(89)90004-X.

- , and M. H. P. Ambaum, 1997: The diabatic contour advective semi-Lagrangian model. *Quart. J. Roy. Meteor. Soc.*, **123**, 1097–1130, doi:10.1002/qj.49712354015.
- Durran, D. R., 2010: *Numerical Methods for Fluid Dynamics*. 2nd ed. Springer, 516 pp.
- Esfahanian, V., S. Ghader, and A. R. Mohebalhojeh, 2005: On the use of the super compact scheme for spatial differencing in numerical models of the atmosphere. *Quart. J. Roy. Meteor. Soc.*, **131**, 2109–2129, doi:10.1256/qj.04.73.
- Galewsky, J. R., R. K. Scott, and L. M. Polvani, 2004: An initial-value problem for testing numerical models of the global shallow-water equations. *Tellus*, **56A**, 429–440, doi:10.1111/j.1600-0870.2004.00071.x.
- Hoskins, B. J., 1991: Towards a PV- $\theta$  view of the general circulation. *Tellus*, **43AB**, 27–35, doi:10.3402/tellusb.v43i4.15396.
- , M. E. McIntyre, and A. W. Robertson, 1985: On the use and significance of isentropic potential-vorticity maps. *Quart. J. Roy. Meteor. Soc.*, **111**, 877–946, doi:10.1002/qj.49711147002.
- Hsu, Y.-J. G., and A. Arakawa, 1990: Numerical modeling of the atmosphere with an isentropic vertical coordinate. *Mon. Wea. Rev.*, **118**, 1933–1959, doi:10.1175/1520-0493(1990)118<1933:NMOTAW>2.0.CO;2.
- Jablonowski, C., and D. L. Williamson, 2006a: A baroclinic instability test case for atmospheric model dynamical cores. *Quart. J. Roy. Meteor. Soc.*, **132**, 2943–2975, doi:10.1256/qj.06.12.
- , and —, 2006b: A baroclinic wave test case for dynamical cores of general circulation models: Model intercomparisons. NCAR Tech. Note NCAR/TN-469+STR, 75 pp., doi:10.5065/D6765C86.
- , and —, 2011: The pros and cons of diffusion, filters and fixers in atmospheric general circulation models. *Numerical Techniques for Global Atmospheric Models*, P. H. Lauritzen et al., Eds., Springer-Verlag, 381–493, doi:10.1007/978-3-642-11640-7\_13.
- Kasahara, A., 1974: Various vertical coordinate systems used for numerical weather prediction. *Mon. Wea. Rev.*, **102**, 509–522, doi:10.1175/1520-0493(1974)102<0509:VVCSUF>2.0.CO;2.
- Konor, C. S., and A. Arakawa, 1997: Design of an atmospheric model based on a generalized vertical coordinate. *Mon. Wea. Rev.*, **125**, 1649–1673, doi:10.1175/1520-0493(1997)125<1649:DOAAMB>2.0.CO;2.
- Lauritzen, P. H., C. Jablonowski, M. A. Taylor, and R. D. Nair, 2010: Rotated versions of the Jablonowski steady-state and baroclinic wave test cases: A dynamical core intercomparison. *J. Adv. Model. Earth Syst.*, **2**, doi:10.3894/JAMES.2010.2.15.
- Lele, S. K., 1992: Compact finite difference schemes with spectral-like resolution. *J. Comput. Phys.*, **103**, 16–42, doi:10.1016/0021-9991(92)90324-R.
- Li, Y., J. Ruge, J. R. Bates, and A. Brandt, 2000: A proposed adiabatic formulation of 3-dimensional global atmospheric models based on potential vorticity. *Tellus*, **52**, 129–139, doi:10.1034/j.1600-0870.2000.00004.x.
- McIntyre, M. E., and W. A. Norton, 2000: Potential vorticity inversion on a hemisphere. *J. Atmos. Sci.*, **57**, 1214–1235, doi:10.1175/1520-0469(2000)057<1214:PVIOAH>2.0.CO;2.
- MirRokni, S. M., A. R. Mohebalhojeh, and D. G. Dritschel, 2011: Revisiting vacillations in shallow-water models of the stratosphere using potential-vorticity-based numerical algorithms. *J. Atmos. Sci.*, **68**, 1007–1022, doi:10.1175/2011JAS3622.1.
- Mirzaei, M., A. R. Mohebalhojeh, and F. Ahmadi-Givi, 2012: On imbalance generated by vortical flows in a two-layer spherical Boussinesq primitive equation model. *J. Atmos. Sci.*, **69**, 2819–2834, doi:10.1175/JAS-D-11-0318.1.
- Mohebalhojeh, A. R., and D. G. Dritschel, 2000: On the representation of gravity waves in numerical models of the shallow-water equations. *Quart. J. Roy. Meteor. Soc.*, **126**, 669–688, doi:10.1002/qj.49712656314.
- , and —, 2001: Hierarchies of balance conditions for the  $f$ -plane shallow water equations. *J. Atmos. Sci.*, **58**, 2411–2426, doi:10.1175/1520-0469(2001)058<2411:HOBFCFT>2.0.CO;2.
- , and —, 2004: Contour-advective semi-Lagrangian algorithms for many-layer primitive-equation models. *Quart. J. Roy. Meteor. Soc.*, **130**, 347–364, doi:10.1256/qj.03.49.
- , and —, 2007: Assessing the numerical accuracy of complex spherical shallow water flows. *Mon. Wea. Rev.*, **135**, 3876–3894, doi:10.1175/2007MWR2036.1.
- , and —, 2009: The diabatic contour-advective semi-Lagrangian algorithms for the spherical shallow water equations. *Mon. Wea. Rev.*, **137**, 2979–2994, doi:10.1175/2009MWR2717.1.
- , and J. Theiss, 2011: The assessment of the equatorial counterpart of the quasi-geostrophic model. *Quart. J. Roy. Meteor. Soc.*, **137**, 1327–1339, doi:10.1002/qj.835.
- Neale, R. B., and Coauthors, 2012: Description of the NCAR Community Atmosphere Model (CAM 5.0). NCAR Tech. Note NCAR/TN-486+STR, 274 pp. [Available online at [www.cesm.ucar.edu/models/cesm1.0/cam/docs/description/cam5\\_desc.pdf](http://www.cesm.ucar.edu/models/cesm1.0/cam/docs/description/cam5_desc.pdf).]
- Simmons, A. J., and D. M. Burridge, 1981: An energy and angular-momentum conserving vertical finite-difference scheme and hybrid vertical coordinates. *Mon. Wea. Rev.*, **109**, 758–766, doi:10.1175/1520-0493(1981)109<0758:AEAAMC>2.0.CO;2.
- Skamarock, W. C., 2011: Kinetic energy spectra and model filters. *Numerical Techniques for Global Atmospheric Models*, P. H. Lauritzen et al., Eds., Springer-Verlag, 495–512, doi:10.1007/978-3-642-11640-7\_14.
- , J. B. Klemp, M. G. Duda, L. D. Fowler, and S. H. Park, 2012: A multiscale nonhydrostatic atmospheric model using centroidal Voronoi tessellations and C-grid staggering. *Mon. Wea. Rev.*, **140**, 3090–3105, doi:10.1175/MWR-D-11-00215.1.
- Smith, R. K., and D. G. Dritschel, 2006: Revisiting the Rossby-Haurwitz wave test case with contour advection. *J. Comput. Phys.*, **217**, 473–484, doi:10.1016/j.jcp.2006.01.011.
- Taylor, M. A., 2011: Conservation of mass and energy for the moist atmospheric primitive equations on unstructured grids. *Numerical Techniques for Global Atmospheric Models*, P. H. Lauritzen et al., Eds., Springer-Verlag, 357–380, doi:10.1007/978-3-642-11640-7\_12.
- Temperton, C., 1984: Orthogonal vertical modes for a multi-level model. *Mon. Wea. Rev.*, **112**, 503–509, doi:10.1175/1520-0493(1984)112<0503:OVNMFA>2.0.CO;2.
- Thuburn, J., 2011: Some basic dynamics relevant to the design of atmospheric model dynamical cores. *Numerical Techniques for Global Atmospheric Models*, P. H. Lauritzen et al., Eds., Springer-Verlag, 3–27, doi:10.1007/978-3-642-11640-7\_1.
- Toy, M. D., and D. A. Randall, 2009: Design of a nonhydrostatic atmospheric model based on a generalized vertical coordinate. *Mon. Wea. Rev.*, **137**, 2305–2330, doi:10.1175/2009MWR2834.1.
- Williams, P. D., 2009: A proposed modification to the Robert-Asselin time filter. *Mon. Wea. Rev.*, **137**, 2538–2546, doi:10.1175/2009MWR2724.1.
- , 2011: The RAW filter: An improvement to the Robert-Asselin filter in semi-implicit integrations. *Mon. Wea. Rev.*, **139**, 1996–2007, doi:10.1175/2010MWR3601.1.